# Dynamic Response of the Fluid Mud to a Tropical Storm

Ge, Jianzhong ; Chen, Changsheng; Wang, Zhengbing ; Ke, Keteng; Yi, Jinxu; Ding, Ping Xing

**DOI**
10.1029/2019JC015419

**Publication date**
2020

**Document Version**
Final published version

**Published in**
Journal Of Geophysical Research-Oceans

JGR Oceans

RESEARCH ARTICLE
10.1029/2019JC015419

# Dynamic Response of the Fluid Mud to a Tropical Storm

**Jianzhong Ge[1,2], Changsheng Chen[3], Zheng Bing Wang[4,5], Keteng Ke[1,6], Jinxu Yi[1], and Pingxing Ding[1]**

[1]State Key Laboratory of Estuarine and Coastal Research, East China Normal University, Shanghai, China, [2]Institute of Eco-Chongming (IEC), Shanghai, China, [3]School for Marine Science and Technology, University of Massachusetts Dartmouth, New Bedford, MA, USA, [4]Faculty of Civil Engineering and Geosciences, Delft University of Technology, Delft, The Netherlands, [5]Deltares, Delft, The Netherlands, [6]Shanghai Investigation Design and Research Institute Co., Ltd., Shanghai, China

**Key Points:**
- A strong fluid mud (FM) formed during the passage of a tropical storm
- A storm-increased stratification initially triggered a massive formation of the FM
- The FM was sustained and transported by saltwater intrusion, and it subsequently broke down during the strong-mixing spring tide

**Correspondence to:**
J. Ge,
jzge@sklec.ecnu.edu.cn

**Citation:**
Ge, J., Chen, C., Wang, Z. B., Ke, K., Yi, J., & Ding, P. (2020). Dynamic response of the fluid mud to a tropical storm. *Journal of Geophysical Research: Oceans*, *125*, e2019JC015419. https://doi.org/10.1029/2019JC015419

Received 26 JUN 2019
Accepted 2 MAR 2020
Accepted article online 10 MAR 2020

**Abstract** Fluid mud (FM) is a unique sedimentary feature in high-turbidity estuaries, where it can make a rapid contribution to morphodynamics. Insufficient field measurements and fixed-point monitoring lead to deficient understandings of the formation, transport, and breakdown of the FM under extreme weather conditions. A field survey was conducted in the Changjiang Estuary during the period of turbidity maximum, just after Typhoon Haikui. The measurements captured the formation of the FM beneath the suspended layers, particularly around the lower reach of the North Passage. The thickness of the observed FM gradually decreased landward along the channel, with the maximum value reaching ~0.9 m. The major features of the observed storm-induced FM were simulated using the Finite-Volume Community Ocean Model. The results indicated that the initial appearance of the FM was the result of a typhoon-intensified, salinity-induced stratification in the outlet region. The subsequent landward propagation of the FM was driven by the combined effects of the FM-induced mud surface pressure gradient force and saltwater intrusion near the bottom. Weak mixing during the subsequent neap tidal period sustained the FM as it rapidly extended into the middle region of the North Passage. This produced a large velocity shear at the interface of the FM and upper suspension layer, increasing the entrainment from the FM to the upper suspension layer. As a result of the increased tidal mixing, the FM weakened and then finally broke down in the subsequent spring tidal period.

**Plain Language Summary** The environment along the large river to estuary continuum is generally turbid and frequently produces highly concentrated benthic sediment suspensions, that is, fluid mud (FM). The FM is a sediment feature, with a concentration mostly in the range of 10 to >100 g/L. It is difficult to track the FM's movement and breakdown. The response of the FM to extreme atmospheric and oceanic conditions is therefore not well understood. In this study, a comprehensive field campaign identified the large-scale formation of the FM after a severe tropical storm in the Changjiang Estuary. The life cycle of the FM in this estuary cannot, however, be determined through the field observation alone. A two-layer FM model was developed to achieve this goal. The experiments suggested that the key physical factor was the stratification resulting from the typhoon-enhanced saltwater intrusion. This led to the formation of the FM in the near-bottom layer. After the FM formed, it extended onshore along the channel under the influence of an ambient saltwater intrusion. The FM was constrained in the benthic layer as a consequence of weak mixing from the saltwater intrusion. The breakdown of the FM was governed by enhanced tidal mixing in the subsequent spring tide.

## 1. Introduction

Fluid mud (FM), which refers to the concentrated benthic suspension, is a distinctive sediment feature in the high-turbidity environment of coastal and estuarine regions, such as the Mississippi River estuary, Amazon River delta, Jiaojiang river mouth, and Changjiang Estuary (Corbett et al., 2007; Guan et al., 2005; Wan et al., 2014; Winterwerp, 1999; Winterwerp & Van Kesteren, 2004; Xie et al., 2010). The FM generally forms an intermittent buffer between an upper relatively low concentration sediment suspension layer and a lower consolidated bed layer. It is an active source for the upper suspension and lower bed layers, as a result of an entrainment process and sedimentation, respectively. It also functions like a sediment sink from the upper

layer by deposition and from the bed layer by erosion (Ge et al., 2018; Winterwerp & Van Kesteren, 2004; X. Yang et al., 2015). The FM can cause a fast sedimentation rate, contributing directly to morphological processes in a high-turbidity estuary.

It is quite difficult to detect the existence of the FM and even more difficult to track its movement and breakdown. The typical sediment concentration within the FM is in the range of 10 to >100 g/L (Winterwerp, 1999). The FM can sustain a very thin vertical thickness, which is not easily resolved through the shipboard observations. Ge et al. (2018) developed a sophisticated monitoring system: a bottom-mounted tripod equipped with various sensors. This system successfully captured the formation and variation of thin FM layers in the Changjiang River Estuary, thus identifying the associated hydro and sediment dynamics.

The FM formation process was simulated using a one-dimensional vertical (1DV) model (Ge et al., 2018; Winterwerp, 2011). However, the FM transport is a three-dimensional (3-D) dynamic process that cannot be resolved just from observations at a few sparsely distributed sites and a 1DV model simulation. Developing a 3-D model is required to examine various rheological behaviors and to replicate the FM, or a FM layer, which then can be observed in either laboratory-scale experiments or realistic estuarine conditions (e.g., Guan et al., 2005; Knoch & Malcherec, 2011; Le Hir et al., 2000; Z. B. Wang & Winterwerp, 1992). The most common 3-D FM models discretize the vertical into a two-layer system consisting of the water column and FM (L. Wang et al., 2008; X. Yang et al., 2015). These models are capable of resolving the FM from the laboratory-scale experiments (Knoch & Malcherec, 2011; X. Yang et al., 2015) and an idealized estuary (Hsu et al., 2009), but only a few have reproduced the FM within or around a realistic geometric river estuary (Guan et al., 2005). Both laboratory experiments and numerical simulations were mainly focused on the hydrodynamics responsible for the FM formation, which included tidal currents, surface waves, and current-wave interactions (Winterwerp et al., 2002).

During the calm weather, the thickness of the FM was observed with a tidally averaged mean value of <0.3 m around the Changjiang Estuary and its adjacent coastal regions (Ge et al., 2018; X. Yang et al., 2015). Under some deposition events, much thicker FMs could occur, evidenced by previously recorded studies of the Waipaoa River shelf, the northern California shelf, the Eel River shelf, the Louisiana shelf, and the Elwha River (Eidam et al., 2019; Hale et al., 2014; Ogston et al., 2000; Traykovski et al., 2000, 2015). However, it is a considerable challenge to monitor and simulate the FM features under extreme weather conditions, particularly during a storm event (McAnally et al., 2007; Wan et al., 2014). A storm can cause rapid changes in currents and surface waves. The fact that the FM is characterized with a lutocline forming ultimately from the rapid settling flux suggests that it could not form under a strong vertical mixing condition. The storm can produce a strong horizontal advection, which can push a newly formed FM into a remote area from its origin and yield the appearance of the FM over there. The FM may be scattered over a wide area and may vary greatly with time. Under a severe weather condition, the formation and movement of the FM can produce a substantial morphological change, which can directly influence estuarine mixing, stratification, and currents. The formation, transport, and breakdown of the FM involve complex 3-D dynamics that cannot be symmetrically understood solely through observations and 1DV model simulation.

To investigate the formation and transport dynamics of the FM in a high-turbidity estuarine environment under an extreme weather condition, we designed a rapid-response field measurement plan for the Changjiang River Estuary. Under this plan we developed a monitoring network with various instruments and sensors that were capable of measuring the spatial distribution of the sediment, water temperature, and salinity, as well as the currents in and around the estuarine tidal channel over a short period of a few hours to up to 1 day after a storm has passed. The measurements were made after Typhoon Haikui. They successfully captured the FM in the high-turbidity zone of the Changjiang River Estuary. The observational data were first analyzed to synthesize the observed features of this FM. Then a two-layer FM sediment model, which was coupled with the latest version of the three-dimensional Finite-Volume Community Ocean Model (FVCOM), was used to examine the dynamics attributing to the formation and transport processes of the observed FM.

This paper is organized as follows. The study sites, measurement configuration, and model development are described in section 2. The FM observations and the corresponding physical processes are presented and discussed in section 3. The model-simulated posttyphoon features of the FM in the Changjiang Estuary are

highlighted in section 4. The physical mechanism and processes as well as some critical issues are discussed in section 5. The major findings and conclusions are summarized in section 6.

## 2. Study Site and Measurement

### 2.1. The Study Site and Typhoon Haikui

The Changjiang River Estuary (Figure 1a) is a high-turbidity estuary connecting to the inner shelf of the East China Sea, with an abundant sediment supply from the upstream region (J. Chen et al., 1999). As a consequence of numerous upstream damming activities, the sediment discharge has significantly decreased from ~$4.0 \times 10^8$ tons/year in 1980s to ~$1.0 \times 10^8$ tons/year in 2000s (S. Yang et al., 2011). The reduction in sediment loading, however, has not changed the strong turbidity maximum nature of this estuary (an enlarged view is shown in Figure 1b) (Li et al., 2018; Wan & Wang, 2017). The formation of the FM is often observed in the estuarine channels, particularly around the high water slack, that is, from late flood to early ebb tidal period (Ge et al., 2018; Wan et al., 2014;).

The North Passage is the major shipping channel in the Changjiang River Estuary. To enhance the shipping capacity, two dikes and dozens of groynes were constructed over the neighboring shoals (Ge et al., 2012; Pu et al., 2015). This passage is fully constrained by the turbidity maximum. Turbulent mixing varies significantly with time and in space along the passage, which could change from a well-mixed condition to a strongly stratified condition over a tidal cycle. It is also the primary meeting place of the freshwater discharged from the upstream estuary and the saline water intruded from the downstream inner shelf, an area suffering from sediment accumulation (C. Chen et al., 2003, 2008; Li et al., 2018; Pu et al., 2015; Wan & Wang, 2017; Xue et al., 2009).

Typhoon Haikui originated southeast of Iwo Jima as a tropical depression and then grew to a tropical cyclone during late July and early August 2012. It was upgraded to a Category-I typhoon on 6 August and made landfall over the Xiangshan region in Zhejiang Province, China, on 8 August (Figure 1a). In the Changjiang River Estuary region, the typhoon caused serious flooding in the coastal region from Shanghai City to Zhejiang Province.

### 2.2. Field Measurement

One day after the typhoon passed, a field survey was conducted around the mouth of the Changjiang River Estuary (Figure 1b). A series of cross-estuarine sections were selected near the North Passage navigation channel, including CS9, CS2, CSW, CS3, CS7, CS4, and CS10. There were two or three ship-anchored sites on each section. Suffix *S* and suffix *N* refer to the sites located on the southern and northern sides of the navigation channel, respectively, while suffix *M* refers to a site located exactly in the middle of the navigation channel. This navigational channel is one of the busiest shipping lanes in the world. For safety, the *M* sites were sampled with a lower frequency than the *S* and *N* sites.

The survey started on 12 August, just 1 day after the typhoon all-clear was declared and ended on 18 August. This field campaign period covered a typical spring tidal (17–18 August), neap tidal (12–13 August), and spring-neap transition cycle (14–15 August). To resolve the spatial distribution of the sediment concentrations, the measurements were made simultaneously on 10 vessels along the main channel of the North Passage (red dots in Figure 1b). The vessels were all equipped with the same types of instruments and sensors, including current meters and water sampling equipment. The Acoustic Doppler Current Profiler with an acoustic sensor frequency of 600 KHz was used to measure the water current profile. The vertical sampling resolution of Acoustic Doppler Current Profiler was specified to be 0.5 m. The salinity and suspended sediment concentration (SSC) were directly sampled at six depths in the water column. These vertical samples were located at relative depths of 5%, 20%, 40%, 60%, 80%, and 95% of the total instantaneous water depth. Three wind-wave buoys were deployed at Niu Pi Jiao (NPJ), Chang Jiang Kou (CJK), and Nan Cao Dong (NCD). These buoys functioned as operational wave platforms. Significant wave height, peak wave period, and wave direction were recorded at an hourly time interval during the typhoon passage (blue dots in Figure 1).

Teledyne Odom Echotrac MK III transducers, with two sonar sensors of high-frequency (220 kHz) and low-frequency (33 kHz), were set up to measure the water depth along the main channel. This measurement was conducted just during a 1-day period on 12 August. The measurement uncertainties were 0.1 m at

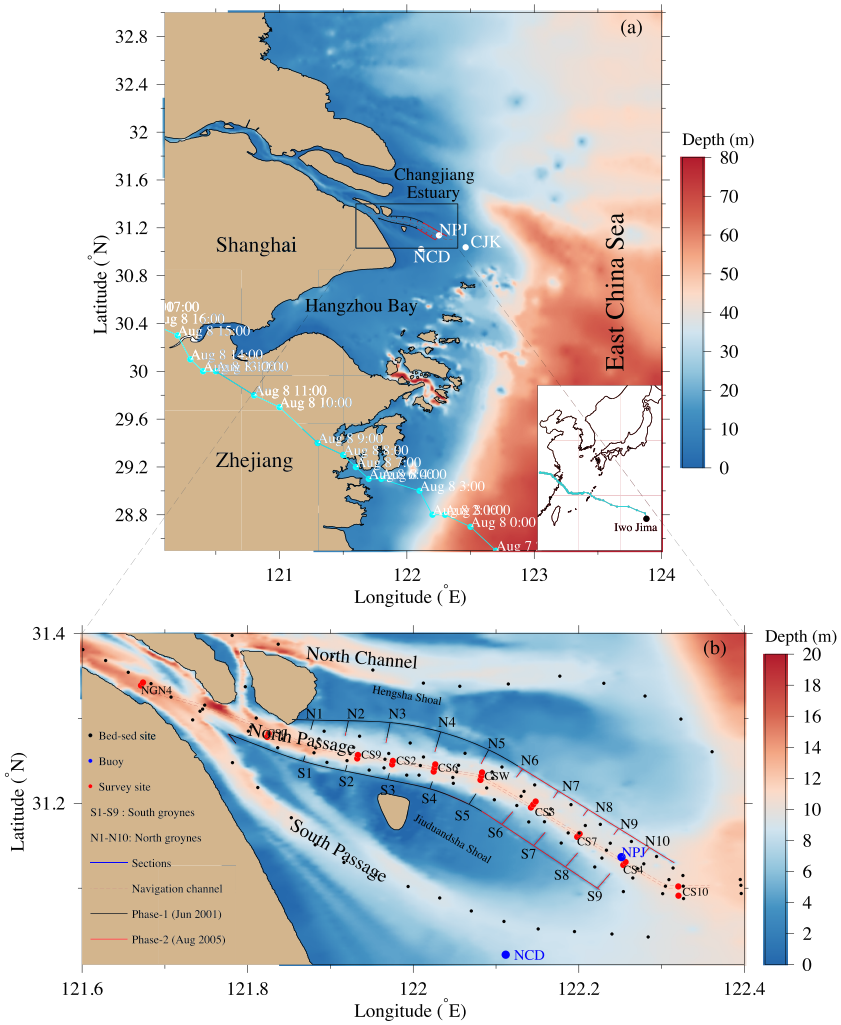


**Figure 1.** (a) Bathymetry of the Changjiang Estuary and the adjacent coastal region, inserted with a panel showing the trajectory of Typhoon Haikui that originated from Iwo Jima during August 2012. (b) An enlarged view of the North Passage with dikes and groynes along the nearby Hengsha Shoal and Jiuduansha Shoal. The dashed red lines represent the navigation channel. The blue dots in two panels indicate the buoy locations for the wind and wave observations. The black dots indicate the sampling sites for the bed sediment. The red dots indicate the mooring survey sites for the hydrodynamics and suspended sediment, which were arranged along cross-channel sections. They are labeled with suffixes *N*, *M*, or *S*, indicating locations in the north, middle, and south of the navigation channel.

33 KHz and 0.01 m at 220 KHz, respectively. The depth differences between the high-frequency and low-frequency sonars were used to estimate the thickness of the FM along the main channel. Since the depth measurements of both acoustic sensors mainly depended on the density gradient near the interface between the water and the FM, a laboratory experiment with the field-collected FM was conducted to calibrate the sound speed and other parameters for the sonar sensors. An additional Stema Systems RheoTune probe was used to measure the density profile in the FM layer for this ground-truthing experiment. This helped us determine the density threshold for the acoustic reflectance of the high- and low-frequency sensors.

Since the FM was formed originally from suspended and bed sediments, it was highly influenced by bed properties. The seabed sediments around the Changjiang River Estuary were sampled simultaneously with the hydrodynamic measurements, starting from 12 August. The sample resolution was relatively high in the North Passage than in the South Passage, North Channel, and other adjacent regions (black dots in Figure 1b). These sediment samples were used to measure the grain size distribution. In particular, the median grain size ($d_{50}$) was measured using the particle laser diffraction method with Beckman Coulter LS13-320.

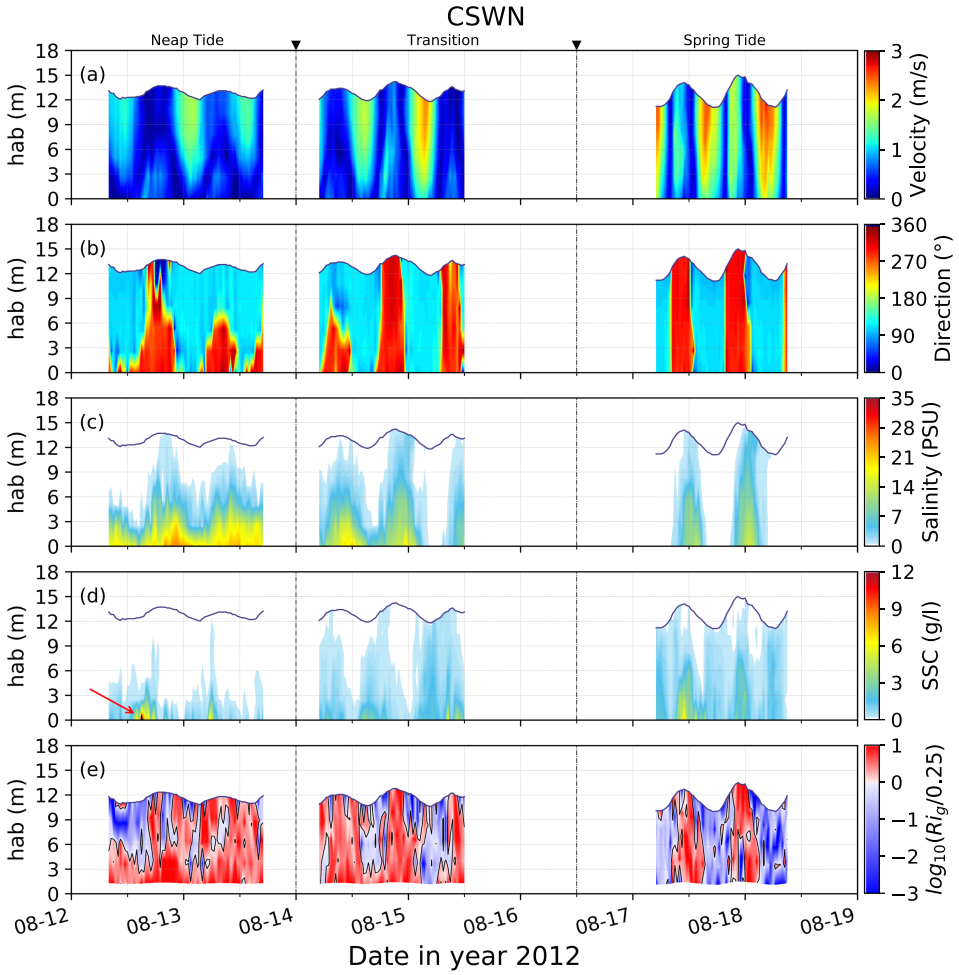


**Figure 2.** Time series of vertical profiles at site CSWN: current velocity (a), current direction (b), salinity (c), suspended sediment concentration (d), and gradient Richardson number (e). Two dashed lines divide the whole duration into the neap tide (12–14 August), transition (14–16 August), and spring tide (16–19 August) periods. The arrow in panel (d) indicates an area where the sediment concentration is greater than 20.0 g/L. The solid lines in panel (e) indicate the zero-value contours.

## 3. Observational Results

### 3.1. Hydrographic Observation

We found that all sites, whether in the northern, southern, or middle areas of the North Passage, exhibited similar temporal patterns (Figure 2). CSWM, a site located in the middle area of the North Passage, was chosen to quantify the physics in the suspension layer. This was a tidally dominant passage with relatively strong vertical velocity shears throughout the water column (Figure 2a). During the spring tide, the maximum velocity was ~3.0 m/s near the surface and ~1.9 m/s near the bottom (Figure 2a), with a surface-bottom difference of ~1.1 m/s. The tidal velocities near the surface and bottom during the neap tide were ~2.2 and ~1.2 m/s, respectively (Figure 2a). The vertical shear of the velocity was thus the same as that found during the spring tide. This strong vertical shear is relevant to the vertical stratification.

The water was strongly stratified during the neap tide and vertically well mixed during the spring tide. During the neap tide, the flow featured a dominant two-layer structure with a difference of ~180° in direction between the surface and bottom. This is evident in Figure 2b, which shows that the water moved seaward with a flow direction of ~115° in the upper layer and landward with a flow direction of ~290° in the lower layer. The direction difference between these two layers was ~175°. This two-layer pattern was clearest at 13:00, 12 August; 13:00, 13 August; and 15:00–18:00, 13 August. As the tidal currents intensified during the spring tide, the tidal-induced vertical mixing weakened the vertical stratification and made the tidal velocity distribution nearly uniform throughout the water column.

**Table 1**
*Sediment Concentrations at Measurement Sites*

| Survey site | SSC range in the upper five layers (g/L) | Maximum SSC in the bottom layer (g/L) | Timing of SSC maximum |
|---|---|---|---|
| CS9S | 0.013–0.853 | 1.46 | S |
| CS9M | 0.023–1.130 | 2.18 | S |
| CS2S | 0.024–1.720 | 7.41 | N |
| CS2M | 0.048–4.860 | 87.80 | N |
| CS6N | 0.021–3.110 | 12.80 | S |
| CS6M | 0.047–4.440 | 69.90 | N |
| CS6S | 0.016–4.670 | 21.80 | S |
| CSWN | 0.005–4.470 | 26.40 | N |
| CSWM | 0.039–8.340 | 48.60 | N |
| CSWS | 0.029–7.930 | 40.70 | S |
| CS3N | 0.005–5.250 | 17.70 | N |
| CS3M | 0.013–5.690 | 77.30 | S |
| CS3S | 0.012–5.510 | 12.30 | S |
| CS7M | 0.030–4.780 | 9.53 | S |
| CS7S | 0.005–9.820 | 14.20 | S |
| CS4M | 0.004–6.920 | 74.50 | N |
| CS4S | 0.002–3.950 | 8.28 | S |
| CS0S | 0.005–0.953 | 1.26 | S |
| CS0M | 0.000–0.216 | 0.23 | N |
| CS10S | 0.003–2.650 | 2.21 | S |
| CS10M | 0.002–1.760 | 87.60 | S |

*Note*. The labels "S" and "N" in the timing column indicate the maximum SSC in the bottom layer, which occurred in the spring and neap cycle, respectively.

The time-varying stratification was verified by the salinity measurements. The vertical profiles of the salinity and SSC showed that the region was generally stratified, particularly around the slack water times during the neap tide (Figures 2c and 2d). At 06:00, 13 August, the salinity near the bottom reached a maximum value of 29.3 PSU. During the spring tide on 18 August, there was a strong tidal current near the surface (Figure 2a). The consequent enhanced vertical shear produced strong mixing and made the water vertically well mixed (Figure 2c).

The SSC showed a similar vertical distribution pattern to the salinity. During the neap tide, the water column was dominated mainly by the low-SSC water, except in the near-bottom layer where the high-SSC was observed. The observed SSC in the upper water column was in the range of 0.1 to 5.6 g/L, while the SSC in the lower water column near the bottom jumped sharply to above 20.0 g/L, with a maximum value of 26.4 g/L (Figure 2d).

The status of stratification is further estimated using the gradient Richardson number ($R_i$):

$$R_i = -\frac{g}{\rho_w}\frac{\partial\rho/\partial z}{\left(\left(\frac{\partial u}{\partial z}\right)^2+\left(\frac{\partial v}{\partial z}\right)^2\right)} \quad (1)$$

where $\rho_w$ is the water density considering the joint effect of salinity and SSC, $\partial\rho/\partial z$ is the density gradient, and $u$,$v$ are the velocity components in the $x$ and $y$ directions. The water column is considered to be stratified when $R_i$ exceeds 0.25. Therefore, $\log_{10}(Ri/0.25)$ is used as an index for the degree of stratification. Figure 2e shows the distribution of the index and reveals that the water column experienced strong and persistent stratification during the neap tidal cycles on 12–13 August, as well as in the transitional period from the neap tide to the spring tide on 15–16 August. During the spring tidal cycles on 17–18 August, the level of stratification showed a rapid variation: The water column was stratified during the flood tidal cycle and well mixed in the ebb tidal cycle (Figure 2e).

Measurements on many other transects, including transects CS2, CS6, CS7, and CS3, showed the same pattern with the same physics (Table 1). In particular, the observed SSC rose to 45.0 g/L and greater at the sites located in the middle channel of the North Passage, with high values at CS2M, CS6M, CSWM, CS3M, CS4M, and CS10M. At several sites, the SSC was found to be greater than 80.0 g/L, suggesting the existence of the FM within the navigation channel in the North Passage. By comparison, the SSC in the upper water column was small, within a general range of 0.0–5.0 g/L and with a maximum value below 10.0 g/L. The strong vertical SSC column gradient indicated that the concentrated suspension was mainly restricted to a layer near the bottom.

### 3.2. Observed FM Distribution

The difference between the depths measured with the low- and high-frequency sonars was used as an indicator of the FM thickness. Using the cruise tracking, recorded along the navigational channel, we plotted the along-channel distribution of the FM thickness (Figure 3a). To estimate the extent of the FM, we divided the shipping channel into 46 units. Each unit was about 2–3 km long and 350 m wide (the approximate width of the shipping channel). The estimated values of the FM thickness were based on a spatial averaging of each unit. The result showed that the FM existed, varying in thickness along the navigation channel from the entrance to the outlet of the North Passage. The thickest FM occurred around the CS4 section in the outlet region, with a maximum value of ~1.0 m at the 36–38 segment positions (Figure 3b). A similar thickness of the FM, about 0.74 m, occurred near CS2. The other sites had relatively low thickness, ranging from 0.05 to

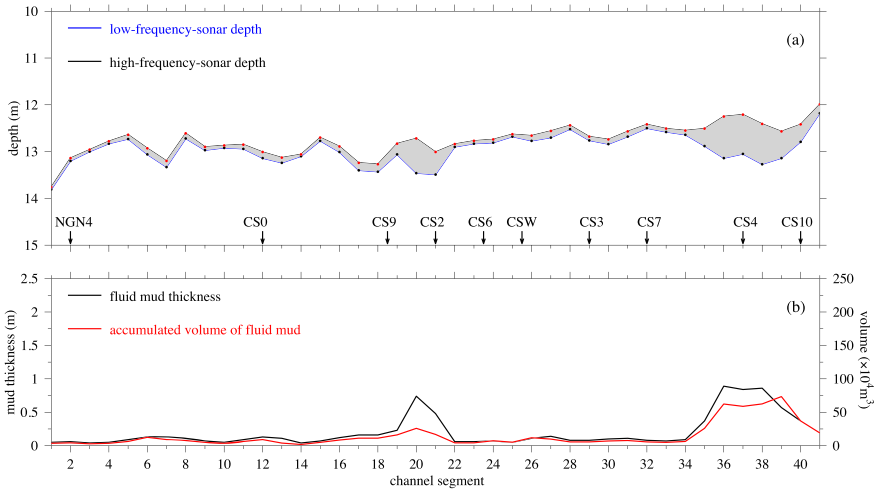


**Figure 3.** The measured depth from low- and high-frequency sonars along the navigation channel (a). The thickness and accumulated FM determined from the depth differences between the sonars (b).

0.23 m. This indicated that a significant FM was detected in the lower reach of the North Passage after the typhoon made landfall.

The volume of the FM was estimated, per section, based on the channel area and the thickness of the FM. The volume peaks tended to correspond with the FM thickness peaks (Figure 3b). The largest unit volumes were ~$7.5\times10^5$ $m^3$ around segment-39 and ~$2.5\times10^5$ $m^3$ at segment-20.

### 3.3. Observed Bed Composition

The spatial distribution of the observed sediment median grain size ($d_{50}$) in the North Passage and adjacent channels showed that this river mouth was mainly covered by fine sediments, with grain sizes smaller than 50 μm (Figure 4a). The upper and lower reaches of the North Passage had even smaller sediment grain sizes. Several patches were classified at 20 μm. The grain size at the centers of these patches was <10 μm. This confirms that the North Passage provided an adequate sediment source for the FM formation. The clay content had a similar distribution of fine sediments. Patches with the smaller grain size corresponded with the high clay component (Figure 4b).

## 4. Numerical Model for FM

### 4.1. The FM Model

To understand the behavioral life cycle of the FM during and after the typhoon had made landfall, FVCOM was configured to simulate the relevant physical processes. FVCOM is a three-dimensional (3-D) unstructured grid primitive equation ocean numerical model (C. Chen et al., 2003, 2006). It discretizes the horizontal space into a triangular mesh and the vertical into terrain-following coordinates. This allowed an accurate geometric fitting for the complex boundaries around the river mouth, particularly for the dikes and groynes within the North Passage. Since these were constructed near the mean sea level, leading to submergence during high water and emergence during low water, the dike-groyne algorithm was activated to better simulate the water and sediment transports over the dikes and groynes (Ge et al., 2012). The latest version 4.3 of FVCOM has integrated the dynamics of the sediment transport as an independent module. This has been shown to be capable of effectively modeling the cohesive sediment dynamics around the Changjiang River Estuary (Ge et al., 2015).

In addition to the original hydrodynamics, sediment, and dike-groyne modules, a two-layer FM model was developed and implemented into the FVCOM sediment module with the aim of resolving and simulating the FM and upper suspension in an estuary. Since the SSC was much greater in the FM than in the upper suspension layer, the complex dynamics were simplified into a two-layer system, with the FM being a thin layer at the bottom of the benthic column that is covered by the low-SSC water. This

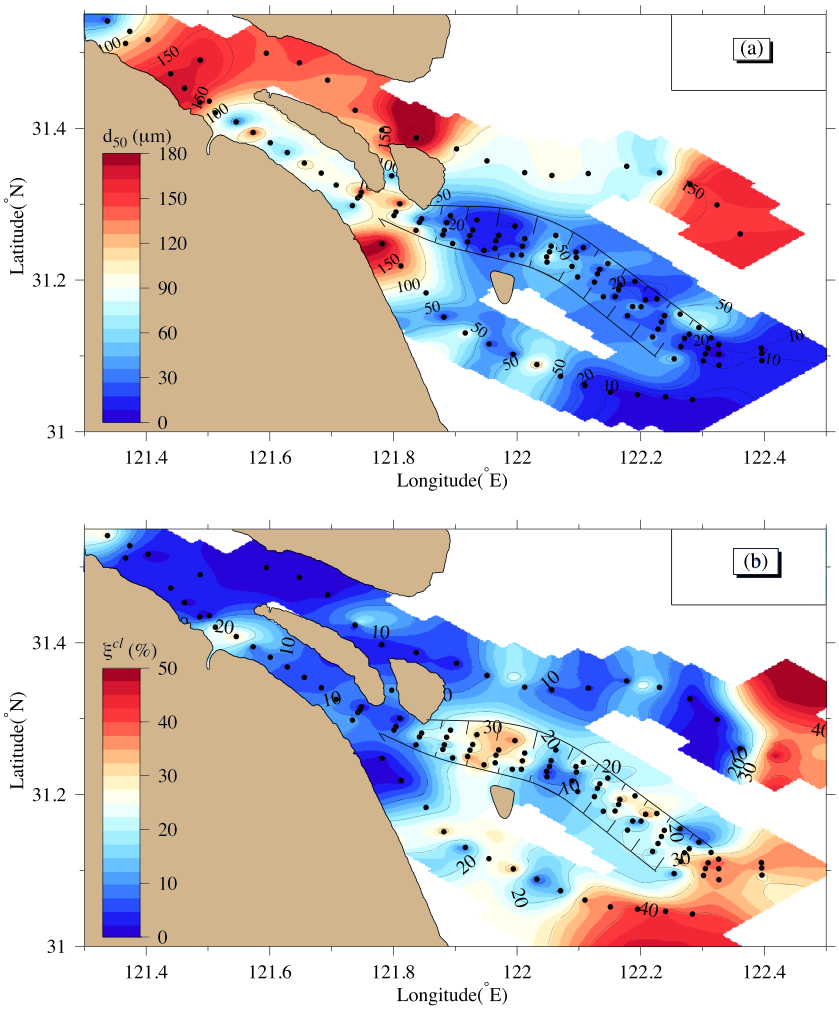


**Figure 4.** Spatial distributions of median grain size $d_{50}$ (a) and percentage of clay content $\xi^{cl}$ (b) of the bed soil sediment. The black dots indicate the soil sampling sites.

simplification was used by Z. B. Wang and Winterwerp (1992) and further used in Winterwerp (1999), Winterwerp et al. (2002), and Ge et al. (2018) within their 1DV or two-layer modeling experiments. Computationally, the model then had three layers: suspension, FM, and seabed (Ge et al., 2018). The suspension layer represented the sediment dynamics for the low-to-medium SSC. The FM was placed between the suspension and bed layers, with a constant sediment concentration and a varying thickness. The seabed layer provided the major source and sink for the suspension and FM layers throughout the vertical sediment exchange.

Winterwerp (1999) outlined a basic three-dimensional framework for the FM flow and its related dynamics (Figure 5). Multiple physical processes occur at the interface between the suspension and FM layers and between the FM and seabed layers. The sediment deposition from the suspension layer and erosion from the bed layer jointly function as the sources that contribute to the formation of the FM. The entrainment process from the FM to the suspension layer and the dewatering effect from the FM to the seabed are the two sinks, leading to the breakdown of the FM (Figure 5). These physical source/sink processes nonlinearly interact in space and with time, thus yielding a variation in the thickness of the FM. The FM also acts as a drag force at the suspension-FM interface. The erosion and deposition processes are controlled by the turbulent kinetic energy in the water column and the shear stress at the bottom produced by the wave-current interaction.

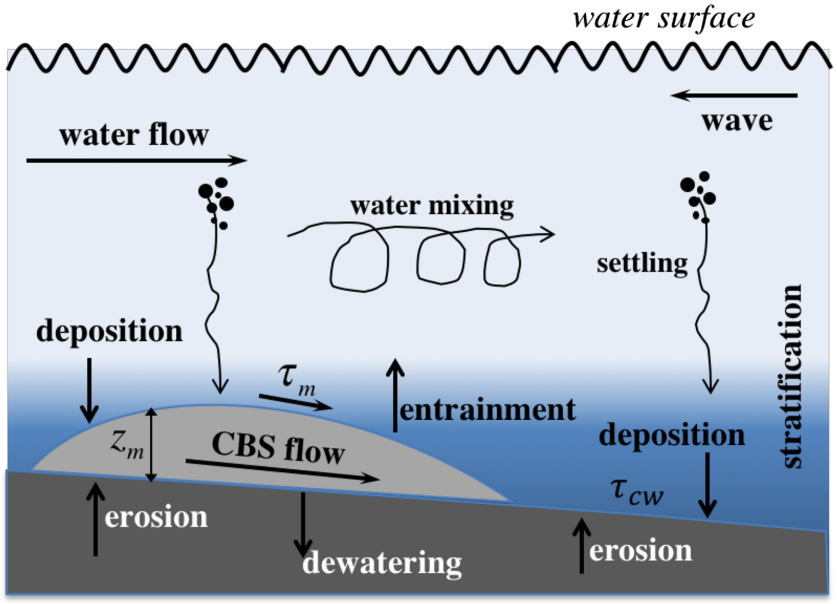


**Figure 5.** Sketch of the physical processes involved in the FM dynamics, modified from Winterwerp (1999). The shaded area indicates the stratification in the water column.

In FVCOM, the sediment dynamics within the upper suspension layer are controlled by advection, diffusion, and particle settling. The governing equations in the water column, following C. Chen et al. (2013), are

$$\frac{\partial C}{\partial t}+\frac{\partial uC}{\partial x}+\frac{\partial vC}{\partial y}+\frac{\partial (w-w_s)C}{\partial z}=\frac{\partial}{\partial x}\left(A_H\frac{\partial C}{\partial x}\right)+\frac{\partial}{\partial y}\left(A_H\frac{\partial C}{\partial y}\right)+\frac{\partial}{\partial z}\left(K_h\frac{\partial C}{\partial z}\right) \tag{2}$$

where $x$, $y$, and $z$ are the Cartesian coordinates; $u$, $v$, and $w$ are the eastward, northward, and upward components of water velocity; $C$ is the sediment concentration; $w_s$ is the settling velocity of sediment particles; and $A_H$ and $K_h$ are the horizontal and vertical eddy diffusion coefficients.

The boundary conditions at the water surface and near the seabed are specified as

$$w_sC+\left(K_h\frac{\partial C}{\partial z}\right)=0, at\ z=\zeta \tag{3}$$

$$w_sC+\left(K_h\frac{\partial C}{\partial z}\right)=ERO-DEP,\ \ at\ z=-H+\Delta z/2 \tag{4}$$

where $\zeta$ indicates the sea surface elevation, *ERO and DEP* represents the eroded and deposited sediment amount through the water-seabed interface, $H$ is the water depth, and $\Delta z$ is the thickness of the bottom discretized layer. The bottom boundary is configured a bit above the bed to avoid $K_h=0$ at the bed surface.

When no FM is generated or transported, the sediment dynamics can be described using equations 2–4. In the vertical direction, the erosion and deposition are the two major physical processes at the interface. When a FM layer is present, the erosion term in equation 4 is replaced by the entrainment term from the FM layer.

When the FM occurs, the governing equations of the FM formation, transport, and breakdown are as presented in Z. B. Wang and Winterwerp (1992):

$$\frac{\partial d_m}{\partial t}+\frac{\partial u_m d_m}{\partial x}+\frac{\partial v_m d_m}{\partial y}=\frac{1}{c_m}\frac{dm}{dt} \tag{5}$$

$$\frac{\partial u_m}{\partial t}+u_m\frac{\partial u_m}{\partial x}+v_m\frac{\partial u_m}{\partial y}+g\frac{\rho_m-\rho}{\rho_m}\frac{\partial \eta_m}{\partial x}-\Omega v_m+\frac{1}{\rho_m d_m}(\tau_{bx}-\tau_{sx})=-\frac{1}{\rho_m}\rho g\frac{\partial \eta}{\partial x} \tag{6}$$

$$\frac{\partial v_m}{\partial t} + u_m \frac{\partial v_m}{\partial x} + v_m \frac{\partial v_m}{\partial y} + g\frac{\rho_m - \rho}{\rho_m}\frac{\partial \eta_m}{\partial y} - \Omega v_m + \frac{1}{\rho_m d_m}\left(\tau_{by} - \tau_{sy}\right) = -\frac{1}{\rho_m}\rho g \frac{\partial \eta}{\partial y} \tag{7}$$

where $t$ is the time; $d_m$is the thickness of the FM layer; $u_m$ and $v_m$ are the eastward and northward components of the FM's horizontal velocity, respectively; $c_m$is the sediment concentration within the FM, which is constant both in height and time; $m$ is the mass of sediment in a unit area; $\rho_m$ is the bulk density of FM; $\rho$ is the density of suspension in the upper layer; $\Omega$ is the Coriolis force acceleration coefficient; $\tau_{bx}$and $\tau_{by}$ are the shear stresses at the FM-bed interface in the $x$ and $y$ directions, respectively; $\tau_{sx}$ and $\tau_{sy}$ are the shear stresses at the suspension-FM interface in the $x$ and $y$ directions, respectively; $\eta_m$is the elevation of the FM; and $\eta$ is the surface elevation of the suspension layer.

The horizontal movement of the FM is affected by multiple processes, including the shear stress on the FM-bed interface ($\tau_b$) and that on the water-FM interface ($\tau_s$), the barotropic pressure gradient force due to the FM surface elevation ($\eta_m$), and the sea surface elevation ($\eta$).

The shear stress at the FM-bed interface is calculated by

$$\begin{pmatrix}\tau_{bx}\\ \tau_{by}\end{pmatrix} = \begin{pmatrix}u_m\\ v_m\end{pmatrix}\frac{\tau_m}{\sqrt{u_m^2 + v_m^2}}, \tag{8}$$

and

$$\tau_m = \tau_B + \frac{f_m \rho_m}{8}\left(u_m^2 + v_m^2\right) \tag{9}$$

where $f_m$ is the friction coefficient between the FM layer and seabed and $\tau_B$ is the Bingham yield strength for the transitional behavior from the Newtonian to non-Newtonian FM, which is set to 0.2 N/m$^2$ (Z. B. Wang & Winterwerp, 1992).

The shear stress at the interface between the FM and suspension layer is determined by

$$\begin{pmatrix}\tau_{sx}\\ \tau_{sy}\end{pmatrix} = \begin{pmatrix}\Delta u\\ \Delta v\end{pmatrix}\frac{f_s \rho\sqrt{\Delta u^2 + \Delta v^2}}{8}, \tag{10}$$

where $f_s$ is the friction coefficient between the FM and the upper suspension layers, $u$ and $v$ are the $x$ and $y$ components of the horizontal velocity in the suspension layer, respectively, and $\Delta u$ and $\Delta v$ are the velocity differences between the upper suspension and FM layers, respectively, and are given by

$$\Delta u = u - u_m \tag{11}$$

$$\Delta v = v - v_m \tag{12}$$

$\frac{1}{c_m}\frac{dm}{dt}$, the right-hand term in equation 5, is balanced by source and sink masses as

$$\frac{dm}{dt} = \text{Settling} - \text{Entrainment} + \text{Erosion} - \text{Dewatering} \tag{13}$$

where Settling and Erosion are the source terms contributing to the formation of the FM and Entrainment and Dewatering act as a sink term for the breakdown effect of the FM.

The Settling is the sediment deposition from the bottom layer of the suspension layer to the FM, which is determined as

$$\text{Settling} = H\left(\frac{\tau_{dm} - \tau_s}{\tau_{dm}}\right) w_s C_b \left(\frac{\tau_{dm} - \tau_s}{\tau_{dm}}\right) \tag{14}$$

where $H()$ is the Heaviside function, $\tau_{dm}$ is the critical shear stress for deposition, and $C_b$is the SSC in the bottom layer of the suspension column above the FM.

Winterwerp (1999) parameterized the entrainment process as follows:

$$\text{Entrainment} = \frac{2C_s\left(|u_{*,m}|^2 - \frac{\tau_B}{\rho_m}\right)\left(\vec{u} - \vec{u}_m\right) + C_\sigma\left(|u_{*,s}|^2 - \frac{\tau_B}{\rho_m}\right)|u_{*,s}|}{\frac{gh\Delta\rho}{\rho} + C_s\left(\vec{u} - \vec{u}_m\right)^2} C_m \tag{15}$$

in which $u_{*,s} = \sqrt[3]{u_*^3 + u_{*,m}^3}$, $u_*$ is the friction velocity of the flow in the suspension layer and $u_{*,m} = f_s(u - u_m)^2$. The empirical coefficients are $C_s = 0.25$ and $C_\sigma = 0.42$. The terms in the brackets are valid only if their values are positive.

The eroded sediment amount is quantified as follows:

$$\text{Erosion} = H\left(\frac{\tau_b - \tau_e}{\tau_e}\right) M_e \left(\frac{\tau_b - \tau_e}{\tau_e}\right) \tag{16}$$

where $M_e$ is the bulk erosion coefficient and $\tau_e$ is the critical shear stress for erosion.$\tau_b$ is calculated depending on these various circumstances: When the FM exists, $\tau_b$ is determined by equation 8. When there is no FM, $\tau_b$ is calculated through the interaction between the wave and current as described in Warner et al. (2008).

The consolidation process from the FM to the seabed is given as follows:

$$\text{Dewatering} = V_0 C_m \tag{17}$$

where $V_0$ is the dewatering rate.

Equations 2–4 govern the upper suspension layer. No matter whether the FM exists or not, equations 2–4 are numerically computed to determine the suspended sediment dynamics. Equations 5–7 are only activated when the model grid resolves the FM. The model was initialized with zero fluid-mud coverage and ran with the inclusion of the fully suspended sediment dynamics. The initial formation of the FM requires reaching a threshold at which the net source/sink term ($\frac{dm}{dt}$) must be positive.

Although this net source/sink term is calculated with four components (equation 13), when no FM appears, both the entrainment and dewatering are zero. $\frac{dm}{dt}$ is determined only by the settling and erosion. If $\frac{dm}{dt} > 0$, it indicates that the settling effect of the suspended sediment is greater than the bed erosion. That is the threshold for the initial formation of the FM from the zero-thickness initialization. It also suggests that the FM forms from a rapid settling of the suspended sediment, not directly from resuspension or bed erosion.

### 4.2. Finite-Volume Discrete Method

Following the main framework of FVCOM, the FM model adopts nonoverlapping unstructured triangular cells for horizontal discretization as described in C. Chen et al. (2003). Since the FM is now treated as a concentration constant and thickness-varying fluid, it can be simulated using a vertically averaged 2-D model. The discretization procedure mainly adopts the 2-D external mode used in the mode-splitting solver in FVCOM. The continuity equation (equation 5), over a control volume, is integrated numerically using the modified fourth-order Runge-Kutta time-stepping scheme. This is a multistage approach with a second-order temporal accuracy. The same method is also used for the integration of equations 6 and 7 to determine the vertically integrated horizontal advection, the barotropic pressure gradient force resulting from the sea surface elevation, the FM elevation, and the Coriolis force. Integration of the barotropic pressure gradient force term can be converted to a trajectory integration using Stokes' theorem. Details of the algorithm for the temporal and spatial discretization are in C. Chen et al. (2013). The formation, movement, and breakdown of the FM could be treated as a typical wet/dry process, like water flooding in FVCOM. In this study, a minimum thickness of 0.05 m was used to determine the wet/dry condition for the FM.

The FM movement, as mentioned above, is driven by the waves and currents acting on the interface and by the slope-induced gravity. The FM height varies significantly as a result of fast changes in the source and sink terms at the interfaces, which produces a FM-induced barotropic gradient force. Solving the continuity and momentum equations of the FM requires a shorter time step than that used for the background

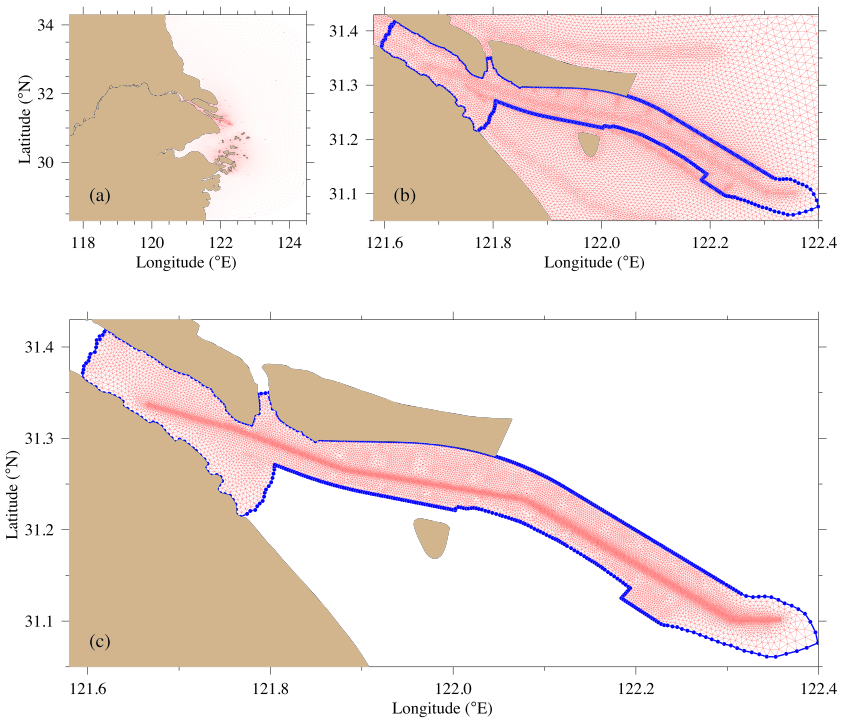


**Figure 6.** The two grids used in the nested modeling. The overall model grid for the Changjiang Estuary and its adjacent coastal regions (a), its enlarged view around the North Passage (b), and the higher-resolution inner model grid within the North Passage (c). The blue curves indicate the nesting boundary between the outer and inner domains.

hydrodynamics and the sediment model. $R_{\Delta t}$ is defined as the ratio of the hydrodynamic external time step to the FM time step.

We observed that the FM was usually generated and moved around in specific, localized areas, such as the center of turbidity maximum or locations where the sediment could be easily trapped due to local bathymetry. This means that the simulation of the FM requires a higher resolution in the regions where there is a high probability of the FM occurrence. For this reason, we configured the model with two nested domains: a large domain covering the Changjiang River Estuary, Hangzhou Bay, upstream Changjiang River, and adjacent coastal regions and a small refined-grid domain covering the North Passage (Figure 6). The purpose of the two-domain nested approach was to balance the local higher resolution with the overall computational efficiency. This method had been proven effective in Ge et al. (2013).

The grid mesh in the large domain mainly followed the previous model grid used by Xue et al. (2009) and Ge et al. (2013). In this study, we have extended the grid mesh about 400 km to the upstream Datong gauge station on the lower area of the Changjiang River. The grid size of this mesh was ~5 km around the open sea boundaries (Figure 6a), decreasing to 500 m near the river mouth (Figure 6b). The small domain was configured with a refined mesh with a grid size as small as 100 m (Figure 6c). The large and small domains were nested in the common grid nesting boundary around the North Passage (blue curves and dots in Figure 6b). The other parameters for the two domains are given in Table 2. The small domain contained 23,351 triangular cells and 12,079 vertices/nodes. A mode-splitting solver was used for the time integration. In this solver, the currents are divided into the external and internal modes that can be computed using two distinct time steps (C. Chen et al., 2013). The time step was 1.0 s for the external mode and 10.0 s for the internal mode in the large domain; this was reduced to 0.5 and 2.5 s for the small inner domain. $R_{\Delta t}$ was set to 10, which indicated that the time step for the FM was reduced to 0.05 s.

In addition, the FVCOM-SWAVE model was used to estimate full wave-current-sediment interactions. The configuration for the wave computations mainly followed Qi et al. (2009) and Wu et al. (2011).

**Table 2**
*Parameters for the Nesting Models*

| | Model for estuary | Model for North Passage |
|---|---|---|
| Cells | 93,848 | 23,351 |
| Nodes | 49,854 | 12,079 |
| Time step for external mode | 1.0 | 0.5 |
| Mode split ratio | 10 | 5 |
| Vertical layers | 20 | |
| Horizontal mixing coefficient | 0.1 | |
| Vertical mixing coefficient | $1.0 \times 10^{-4}$ | |
| $\tau_{dm}$ | 0.1 N/m$^2$ | |
| $C_m$ | 200 g/L | |
| $M_e$ | $2.0 \times 10^{-4}$ kg/(m$^2$/s) | |
| $C_s$ | 0.25 | |
| $C_\sigma$ | 0.42 | |
| $f_s$ | 0.032 | |
| $f_m$ | 0.05 | |
| $\tau_{ce}$ | 0.2–1.8 N/m$^2$ | |
| $\omega_s$ | 0.6 mm/s | |
| $\rho_m$ | $1.1 \times 10^3$ g/L | |
| $\rho_s$ | $1.0 \times 10^3$ g/L | |
| $V_0$ | $4.0 \times 10^{-6}$ m/s | |
| $R_t$ | 10 | |

The model was driven by multiple external physical forcings. Daily freshwater discharge from the Changjiang River was considered at the upstream modeling boundary (data source: www.cjh.com.cn). A total of 10 major astronomical tidal components was specified at the lateral boundaries, including four diurnal tides (K1, O1, P1, and Q1), four semidiurnal tides (M2, S2, N2, and K2), and two quarter diurnal tides (M4 and MS4). The surface atmospheric forcing was provided by the ERA-Interim data from the European Centre for Medium-Range Weather Forecast (ECMWF). It had a 0.125° spatial resolution and a 3-hr temporal resolution.

### 4.3. Model Validation and Sensitivity

The model was validated for the tidal elevation and currents, residual flow, salinity, and sediment concentration in previous studies (Ge et al., 2013, 2015). The same types of model-data comparisons were made in this study. Here, we focus on the model-data comparison of the winds, waves, and sediments.

We first compared the ECMWF wind with the observed wind recorded on three buoys named CJK, NPJ, and NCD (Figures 7a–7c). The ECMWF-derived wind showed a reasonable match with the observed wind, particularly the wind peaks during the typhoon landfall on 8 August. The wind gusts reached ~25 m/s at CJK (Figure 7a) and ~20 m/s on the other two buoys (Figures 7b and 7c). The root-mean-square errors at CJK, NPJ, and NCD were 2.9, 1.67, and 1.69 m/s, respectively. Our comparison indicated that the ECMWF-derived wind was robust, with a reasonable accuracy, in the Changjiang Estuary during the survey period.

The SWAVE-simulated significant wave height was directly compared with the observed significant wave height recorded on the buoys. The root-mean-square errors at CJK, NCD, and NPJ were 0.52, 0.34, and 0.65 m, respectively. The results showed that SWAVE not only accurately reproduced the observed significant wave heights but it also well captured the wave propagation in the Changjiang River Estuary during the typhoon (Figure 7). Both SWAVE and the observations had a maximum significant wave height ($H_s$) of ~4.5 m on CJK (Figure 7d) and of ~3 m on NPJ and NCD (Figures 7e and 7f). The ECMWF-derived wind showed no significant difference among the three buoys, but $H_s$ decreased significantly, by 1.5 m, from CJK to NPJ and NCD. This suggests that the typhoon produced strong swells that propagated toward the

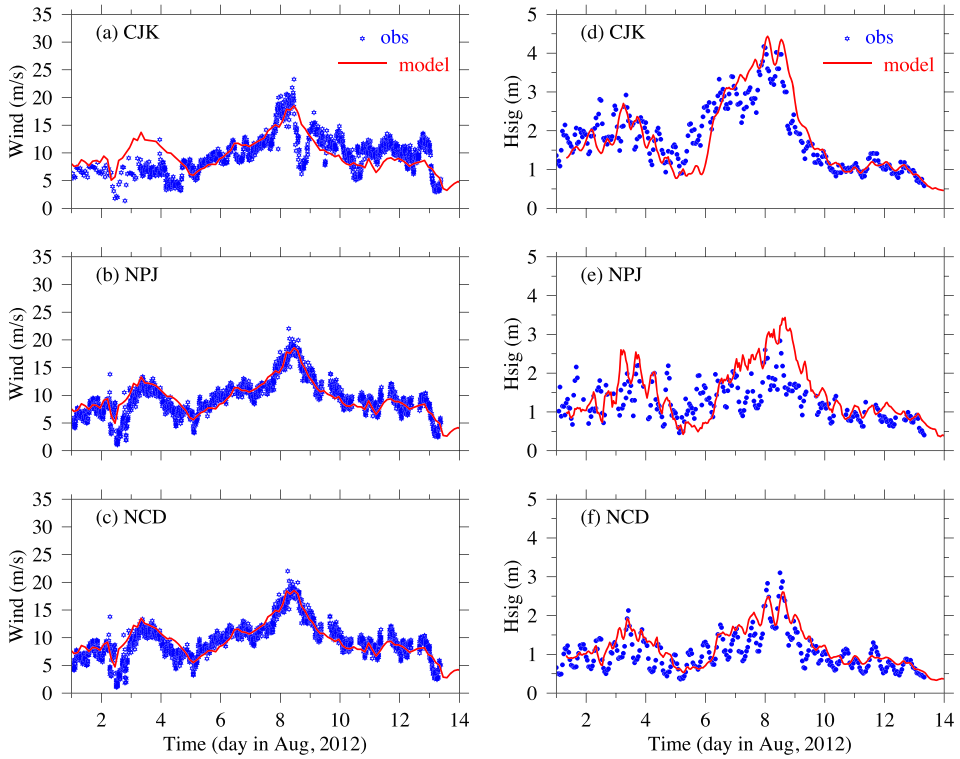


**Figure 7.** The model-data comparisons for wind speed at 10-m height (a–c) and significant wave height (d–f) at buoys CJK (upper row), NPJ (middle row), and NCD (lower row). The blue stars and red curves indicate observed and modeled results, respectively.

Changjiang River Estuary, which dissipated rapidly after reaching the dike and groyne area. The good agreement between the model-simulated and observed waves led us to believe that our model was capable of capturing the nonlinear wave-current interaction during the typhoon passage. Combining the water velocity data with the surface wave data, we found that the significant wave height was larger during the high tide and lower during the low tide. This was caused by white capping, as well as the bottom friction, which led to the energy dissipation (J. Chen et al., 2018). During the low tide, the shallower depth caused larger friction, which suppressed the wave propagation.

The two-layer model characterized the whole water column into two parts: an upper low-SSC suspension and a lower FM. For the FM layer, it was described as a constant concentration mud column. Due to our assumption of a constant concentration mud column, the model cannot directly simulate the mud concentration. For this reason, we assessed the model by the model-data comparison for the upper SSC and the FM thickness separately.

The sediment model was validated by Ge et al. (2015) through direct comparisons of the sediment concentration in the suspension layer. In this study, the comparison was focused on the FM between the suspension and seabed layers. The model-simulated and observed sediment concentrations were in good agreement at the different measurement depths over the spring-neap tidal cycle (Figure 8). The model successfully reproduced the low-SSC region at NGN4S (Figures 8j–8l) and the high-SSC turbidity maxima at CS3S (Figures 8a–8c), CSWN (Figures 8d–8f), and CS7S (Figures 8g–8i). The model also nicely resolved the SSC variation in the upper column above the middle depth. However, it failed to capture some peaks that suddenly appeared near the bottom. For example, the SSC records showed a rapid SSC increase at CSWN (Figure 8f) during the neap tide and at CS7S during the tidal transition period (Figure 8i). These SSC peaks had the same magnitude as those found during the spring tide and were probably caused either by the mixing effect between the FM and the suspension layers or by oscillations of the FM surface. This near-bottom area of the upper suspension column was affected by the lower FM, leading to greater SSC in the bottom region of the suspension column. This feature, however, was not captured in the model. In the numerical

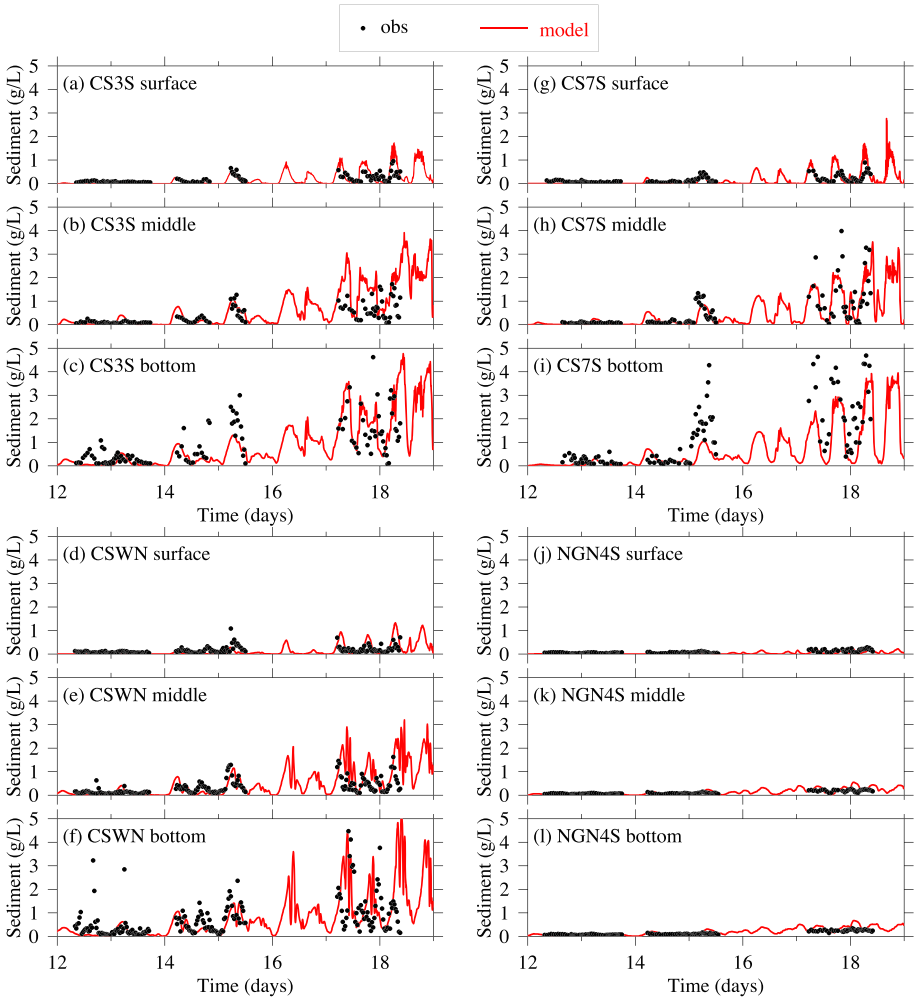


**Figure 8.** Model-data comparisons between the simulated (red curves) and directly sampled (black dots) suspended sediment concentrations in surface, middle, and bottom layers at sites CS3S (a–c), CSWN (d–f), CS7S (g–i), and NGN4S (j–l).

model, the upper suspension was calculated through relatively low SSC sediment dynamics. That was the reason that the model was unable to reveal the greater SSC pulse.

The model-simulated distribution of the FM thickness along the navigation channel was also compared with the observed data (Figure 9a). Since the measurements were made during the cruise survey on 12 August, the comparison was made based on the 24-hr averaged FM thickness on that day. The comparison showed that the FM model reasonably matched the major distribution pattern of the FM, particularly at the sites from CS7 to CS10 in the lower reach of the North Passage: The region of the FM occurrence was well reproduced. The model-simulated FM thickness was about 1.6 m. In this region, although the model results had more peaks and troughs, it produced magnitudes similar to the observation. Considering that these measured data were the averaged values measured on the cruise over a 2- to 3-km distance, the FM model robustly captured the dynamics of the FM formation.

The FM model contained various prescribed parameters (listed in Table 2), such as the sediment concentration within the FM ($C_m$), the friction coefficients at two material interfaces ($f_s$ and $f_m$), and the dewatering efficiency ($V_0$). The modeling sensitivity for the FM layer could be assessed. The model was configured with different settings for these parameters. The $f_m$, $f_s$, and $V_0$ were set to +10% larger and −10% smaller than the original configuration shown in Table 2. The $C_m$ was specified as +5% larger and −5% smaller.

The sensitivity-testing results are shown in Figure 9b. They indicate that the FM model was not sensitive to $f_m$and $f_s$. With smaller changes, these two parameters demonstrated weak or moderate fluctuations,

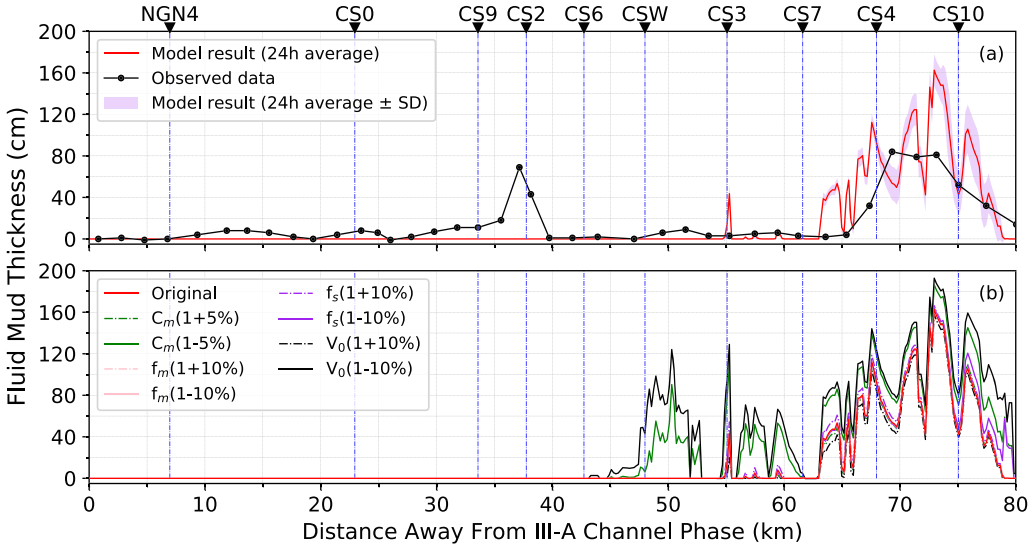


**Figure 9.** (a) Model-data comparisons of the thickness of the FM along the navigation channel. (b) Model sensitivity results for various parameters and configurations, including $V_0(1 \pm 10\%)$, $f_s(1 \pm 10\%)$, $f_m(1 \pm 10\%)$, and $C_m(1 \pm 5\%)$. The data thickness uses the 1-day averaged measurements from 12 August 2012.

compared with original results. By contrast, the dewatering velocity and mud concentration showed significant sensitivity during the FM modeling. Particularly, a smaller $C_m$ and $V_0$ could produce a much thicker FM layer. There was approximately a 20-cm increase in the thickness of the FM layer from CS7 to CS10 and the outer region (Figure 9b). The FM could be extended to the CSW-CS3 region under these two conditions. The increase of $C_m$ and $V_0$ could lead to a smaller prediction for the thickness of the FM layer.

## 5. Formation, Transport, and Breakdown of FM

The tidal current, waves, suspended sediment, saltwater intrusion, and mixing via stratification were major physical processes in the Changjiang River Estuary. These processes nonlinearly interacted with each other and mutually led to the formation, extension, and breakdown of the FM. Using a two-layer FM model, we analyzed the relative contributions of these individual processes, noting especially their effects on the temporal and spatial variations of the FM.

### 5.1. Formation of FM

At selected sites in the middle of the navigational channel, from the inner CSWM and CS7M to the outer CS4M and CS10M, the time series of the simulated FM thickness clearly showed that the FM originally formed in the outlet region of the North Passage and then propagated landward into the upstream channel (Figure 10). The FM first appeared at CS4M at the end of 5 August, then gradually increased in thickness starting from 7 August, 1 day before the typhoon landed, and finally reached a peak thickness of ~120 cm on 10 August (Figure 10c). A similar pattern was observed at CS10M, with a few hours' time lag relative to CS4M (Figure 10d). At this site, the maximum FM thickness was ~175 cm, which occurred on 10 August, nearly 2 days after the typhoon landed. At the inner site CS7M, the FM formed with a 2-day delay (Figure 10b), and its thickness was never as high as that at the outer CS4M and CS10M locations. Also, at this CS7M site, the maximum FM thickness was less than 1.0 m and oscillated significantly, suggesting that the FM was influenced by strong local source/sink effects and by lateral transport. The site CSWM, however, did not show any occurrence of the FM (Figure 10a). This result was in good agreement with the observations (Figure 9a).

The time evolution of the FM also showed a remarkable tidal influence. Four typical snapshots, T1 to T4, were selected for this analysis, which covered the main period of the FM occurrence (Figure 10). When the typhoon-induced strong wind swept through the North Passage, $H_s$ increased significantly after T1. The FM accumulation started on 8 August, and the maximum $H_s$ occurred when the typhoon reached its closest position to the North Passage (Figure 10). T1 was the time at which a significant FM formed at

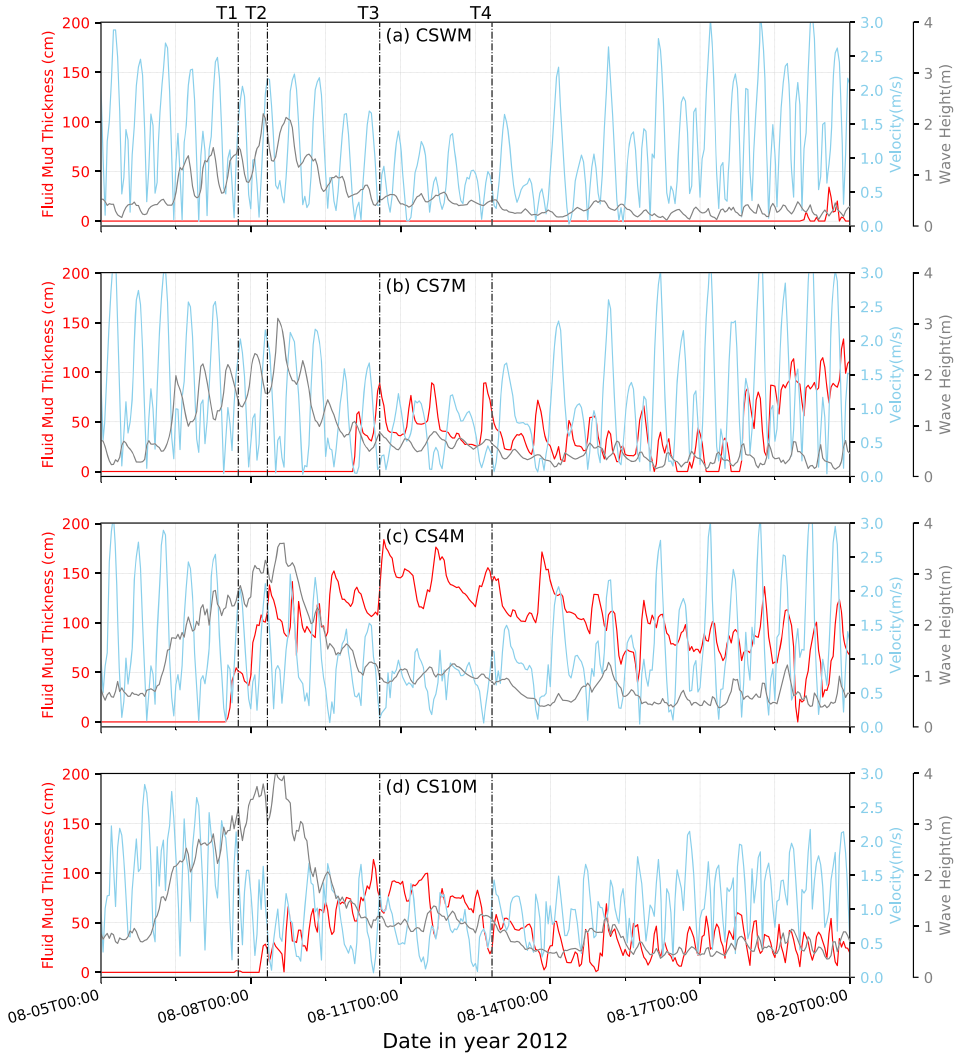


**Figure 10.** The time series of simulated thickness of the FM (red curves), significant wave height (black curves), and tide current velocity (blue curves) from 5 to 20 August at selected middle-channel sites CSWM (a), CS7M (b), CS4M (c), and CS10M (d). T1, T2, T3, and T4 are four selected timings at 7 August 2012, 18:00:00; 8 August 2012, 08:00:00; 10 August 2012, 14:00:00; and 12 August 2012, 20:00:00, respectively.

CS4M within the North Passage. Then CS10M was covered by the FM shortly thereafter at T2. The formation stage can thus be determined by the time duration from T1 to T2.

Snapshots at the formation stage (T1 to T2) of the FM were used to determine the spatial variability of the FM (Figure 11). It was clear that the FM started to form around CS4M and CS10M in the outlet region of the North Passage at 18:00, 7 August, with its thickness rapidly reaching ~65 cm in the initial stage before the typhoon made landfall (Figure 11a). The FM then significantly accumulated and covered the channel area from CS4M to CS10M at T2 (Figure 11b). Snapshots of the SSC on an along-channel section overlapped with the FM and water movement velocities, showing that at the initial stage of the FM formation, the lower part of the water column, in the lower reach of the North Passage, was occupied by the high-concentration sediment suspension (Figure 12a). The SSC concentration was mainly >4 g/L, with a value of >8 g/L near CS10M. As a result, a thick FM formed near CS10M at T1 (Figures 11a and 12a). At this time, the tidal current flowed seaward and pushed the FM in the same direction. Near the bottom, however, the tidal current was only ~0.1–0.2 m/s, so its influence on the FM movement was weak. This explains why the velocity of the FM layer was only ~0.05 m/s and why the whole FM layer was relatively thin.

At T2, when the typhoon-induced maximum wind occurred, the strongest surface wave created much greater SSCs in the suspension layer in the lower reach of the North Passage (Figure 12b). Mixing was

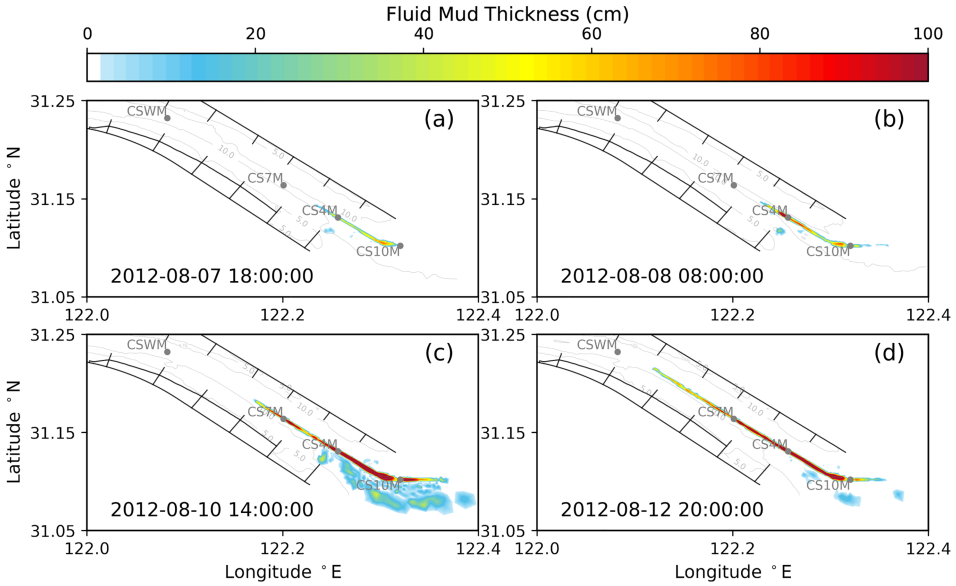


**Figure 11.** Spatial distribution of the FM thickness within the North Passage at T1 (a), T2 (b), T3 (c), and T4 (d). The black dots indicate the selected survey sites.

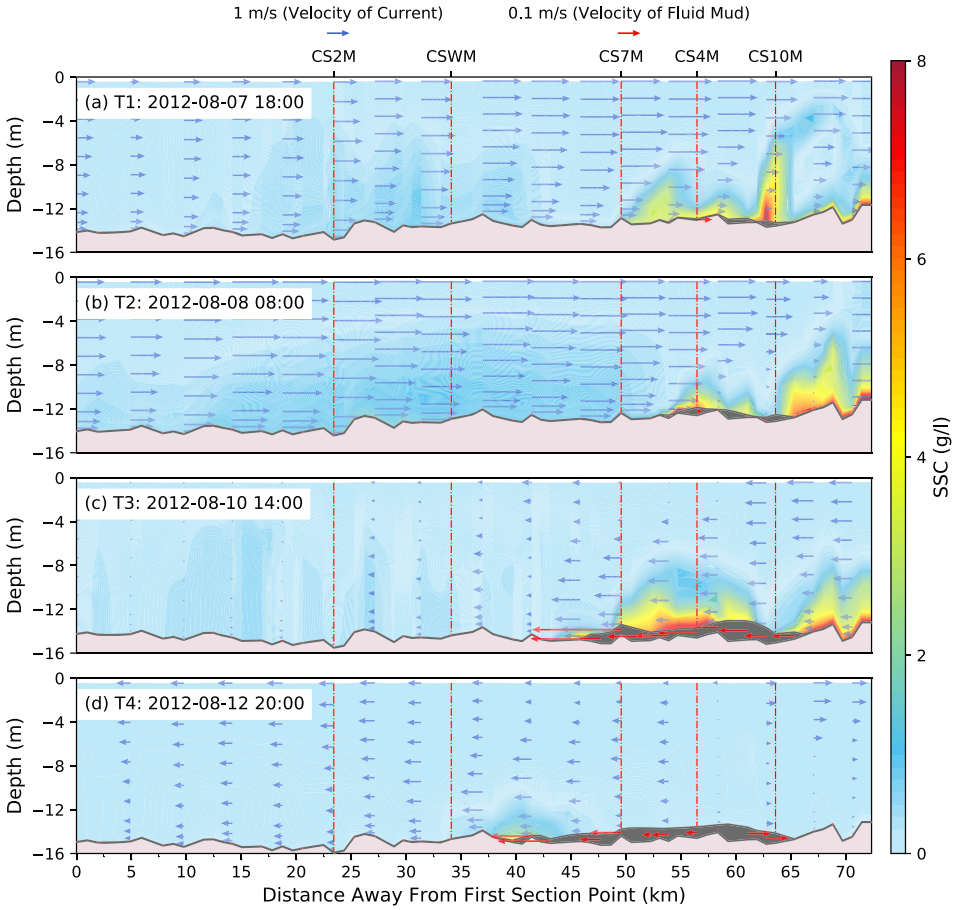


**Figure 12.** Vertical distributions of the currents and SSC along the navigation channel at T1 (a), T2 (b), T3 (c), and T4 (d). The dark shaded areas indicate the corresponding distribution of the FM thickness along the channel. The blue and red arrows indicate the tidal current and FM flow, respectively. The arrow length and head size are scaled to the current velocity.

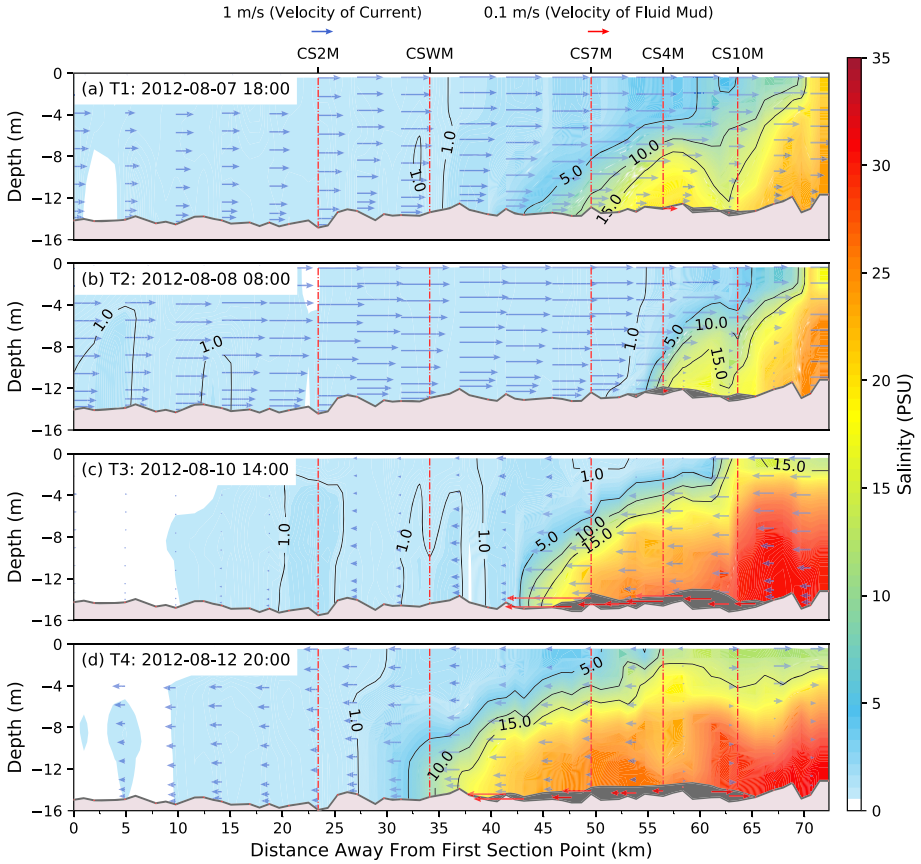


**Figure 13.** Same as Figure 12 except that the colors indicate salinity.

significantly enhanced by the wave-current interaction process. As a result, the high-SSC water not only dominated the bottom but also entrained into the middle of the water column. The FM then flowed upstream, following the ambient tidal flow. Under these conditions, the FM flow velocity was ~0.2 m/s near CS4M.

In this study, the stratification was estimated based on the salinity front in the water column. Along the channel section, the vertical distribution of the FM and corresponding salinity indicated that there was a strong saltwater intrusion into the North Passage (Figure 13). In the early and growing stages of the FM during the moderate tide, the salinity front was not very strong. The vertical salinity gradient was also not very large, suggesting that the tidal mixing was still significant during this period (Figure 13a). At T2, under a similar tidal condition, the water remained vertically well mixed (Figure 13b).

The typhoon caused the strong impact on the various dynamics mentioned above, including the waves, flow, and stratification. To determine the triggering physical processes leading to the FM formation, three additional numerical experiments were made. The first experiment considered the effect of the typhoon wave on the flow, sediment, and FM. In this experiment, the typhoon wave forcing was not included in the hydrodynamic modeling. We called this the no-wind case. The second experiment considered the effect of the typhoon wind on the hydrodynamics, but the wave impact was not included. We call that the no-wave case. The third experiment considered the effect of both the typhoon-induced wind and wave on the flow, suspended sediment, and FM. In this experiment, no stratification was taken into account, so we called it the barotropic case. In all the three cases, the water column sediment and FM models followed the configuration shown in Table 2 without any modifications.

Taking the formation process at CS4M as an example, the results of these three experiments are shown in Figure 14, and they were compared with the result from original simulation shown in Figure 10c. We found that the wave was not an essential factor for the FM formation. Without the wave impact, the FM could still

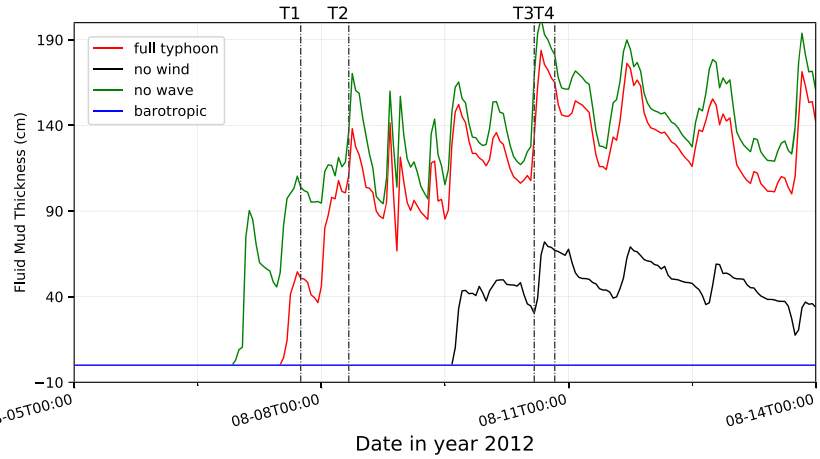


**Figure 14.** The time series of the simulated thickness of the FM from the original (red curve), no-wind (black curve), no-wave (green curve), and barotropic (blue curve) cases.

form and grow thicker. The thickness of the FM was about 10 cm higher compared with the original simulation result. In this case, the near-bottom shear stress was smaller, suggesting a weaker turbulent energy at the FM-suspension interface. It led to a weaker entrainment and thus a thicker FM layer.

The results from the no-wind and barotropic cases suggested that the stratification was the key physical process leading to the FM formation. The no-wind condition was still able to produce a significant formation of the FM, with a magnitude of ~40–70 cm. In this case, the FM occurred after 3 days. This result implied that the FM could form even without the typhoon wind's impact. The barotropic case, however, showed no FM generation, regardless of whether or not the typhoon-induced wave and wind were activated. The only difference between the no-wind and barotropic cases was the level of stratification. Therefore, the stratification was deemed a necessary condition to trigger the FM formation.

The no-wind and original experiments suggested that the typhoon wind did have a significant influence on the massive formation of the FM. The strong surface wind significantly modified the flow condition and stratification. Under the no-wind condition, the distributions of the flow and salinity along the channel showed that the saltwater intrusion was much weaker than that in the original simulation. The isohalines in the no-wind scenario had greater extension at the selected four snapshots. At T1, the isohalines of 5.0 to 15 PSU at the intrusion front covered an approximate length of 15 km of the channel (Figure 15a). Whereas in the original simulation, the along-channel length covered by these isohalines was less than 10 km. In the vertical, the salinity gradient at CS10M was much stronger in the original case than in the no-wind case. For the other three selected times, the salinity gradients around the intrusion front were much stronger under the condition with a full typhoon impact (Figures 13b–13d) than that in the no-wind scenario (Figures 15b–15d). The thickness and FM coverage were both smaller than that in the case with the typhoon. In fact, the typhoon wind strongly enhanced the saltwater intrusion and thus intensified the degree of stratification. Therefore, the stratification was the key physical process producing the massive formation of the FM.

Previous observational and modeling studies have confirmed that stratification via vertical mixing has strong effects on the FM dynamics (Ge et al., 2018; Geyer, 1993; Winterwerp, 1999;). Additionally, in an estuary, the lateral and vertical mixing between the low-salinity freshwater and high-salinity sea water can create complicated haloclines and establish a baroclinic pressure gradient force. The salinity-induced density gradient, in turn, suppresses the production of turbulent kinetic energy in the water column and hence weakens vertical mixing (Geyer & Ralston, 2011), which can greatly modulate suspended sediment advection and diffusion (Ge et al., 2018; Liu et al., 2011; Ren & Wu, 2014).

### 5.2. Transport of FM

After the FM began to form, the astronomical tides transitioned from the spring phase (T2) to the neap phase (T3). This period was defined as an extension stage of the FM. During the time from T2 to T3, the

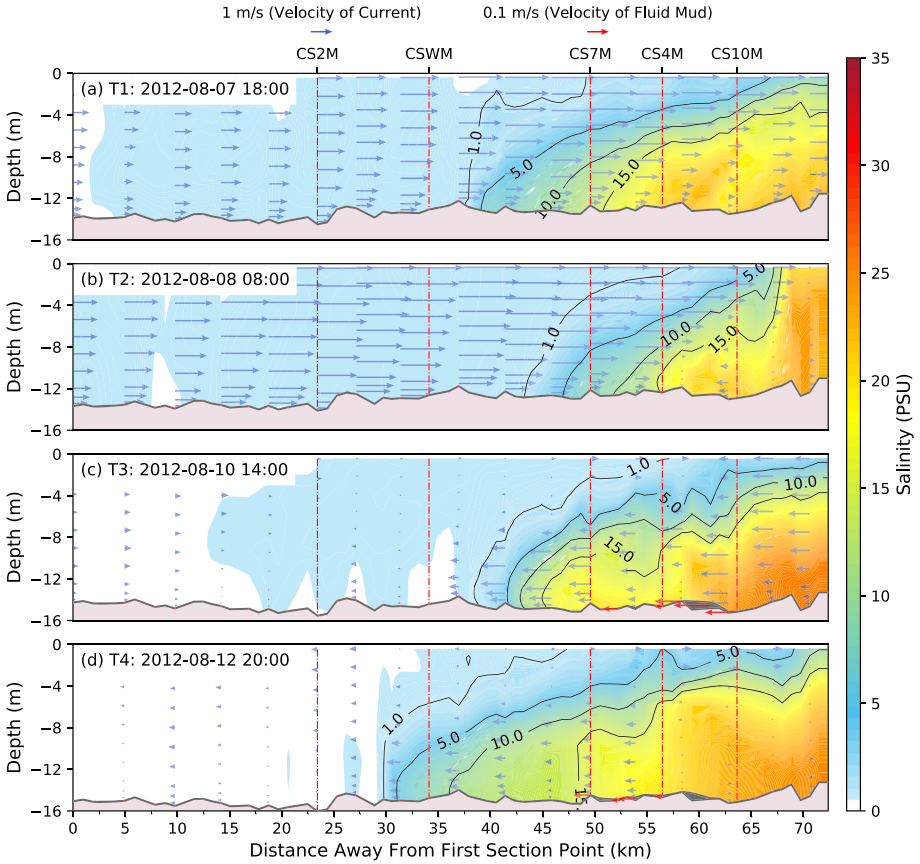


**Figure 15.** Same as Figure 13 except that modeled results are from the no-wind case.

near-bottom flow reached ~1.5 m/s at all four sites, suggesting strong tidal mixing in that region, followed by the FM thickness oscillations at CS10M, CS4M, and CS7M (Figure 10). It expanded seaward along the channel and also gradually propagated upstream, with the FM center shifting to the channel near CS4M and finally reaching CS7M (Figure 11c). The maximum thickness was above 1.5 m at CS4M, but dropped to 70 cm at CS10M, and was 83 cm at CS7M. By T3, however, the FM appeared as isolated patches in the northern shoal, with a thickness of 15–50 cm. This explained why a high SSC was observed at the shoal sites during the field campaign (Table 1), suggesting that the FM could have formed and been transported into the shallow shoals.

At T3, the FM thickness reached its maximum. At this time, the SSC significantly decreased, but the high-SSC bottom water was still visible in the suspension layer (Figure 12c). A relatively strong flow was found in the lower column around CS7M, with a velocity of about 1.0 m/s near the bottom and of almost 0 near the surface. This caused the FM to flow at a higher speed. The velocity reached 0.4 and 0.1 m/s at the onshore extension FM head and tail, respectively.

During the neap tide, the saltwater intrusion extended upstream into the middle area of the channel. At T3, the FM thickness reached its maximum value and the salinity front reached the area near CS2M (Figure 13c). The near-bottom layer around the middle area near CSWM was dominated by high-salinity water (Figure 13d).

It was found that the FM locations highly correlated with the salinity haloclines in the saltwater intrusion front. The FM extension mainly followed this front (Figure 13). It can be inferred that the salinity-induced stratification was a major factor in the maintenance of the high SSC in the suspension layer and in the FM formation. This relationship was suggested by previous studies in the Changjiang River Estuary (Ge et al., 2018; Li et al., 2018 Wan & Wang, 2017), in similar dynamic regions in the Magdalena River of Colombia (Restrepo et al., 2018), and in the Rhine-Meuse estuary (De Nijs & Pietrzak, 2011).

Stratification could also be enhanced by sediment distribution (Ge et al., 2018; Geyer, 1993; Winterwerp, 2002, 2006). The high SSC in the suspension layer corresponded with the salinity intrusion front and strongly influenced the near-bottom part of the water column (Figure 12). With a high SSC above the FM (Table 1), the sediment-induced vertical density gradient was strong, thus intensifying the stratification. The combined effect of salinity and sediment weakened the vertical mixing that produced the extension of the FM at the salinity intrusion front. Therefore, under the extension stage, the transport of the FM was consequently controlled by the saltwater intrusion, and the extension edge of the FM was constrained within the salinity front.

### 5.3. Breakdown of FM

On 8–9 August, after the typhoon passed, the tidal flow transitioned to the neap phase from T3 to T4. At these three sites, the FM thicknesses all reached their maximum values within the neap tide. Also over this period, $H_s$ dropped substantially, and the flow reached a minimum of 1.0 m/s at all three sites.

At T4, the SSC in the suspension layer significantly decreased. Under the weak tidal and wave conditions in the neap tide, the SSC in the channel was low (Figure 12d). The FM movement still followed the ambient tidal flow and saltwater intrusion (Figure 13d). The head of the FM body showed a rapidly landward movement as it arrived at a location near the CSWM and a seaward movement as it arrived at a location near the CS10M. As a result, the FM was more evenly distributed along the channel.

Although the FM reached its maximum during the neap tide, it showed a decreasing trend over the period from T3 to T4. Therefore, it experienced the breakdown stage after T4. After the neap tidal period, the tidal flow gradually increased. On 15 August, the magnitude of the tidal velocity was 1.5 m/s during the neap-spring transition; then on 17–18 August, it rose to ~3.0 m/s during the spring tide. During this period, $H_s$ was low, at about 0.5 m in the outlet area and 0.25 m at CSWM (Figure 10). Under these physical conditions, the FM continued to diminish. It almost disappeared on 17 August. After that, the weakened FM was only visible at CS4M and CS10M, with a thickness of <50 cm. This was consistent with the SSC measurements, which showed an extremely high SSC of 87.6 g/L during the spring tide (Table 1).

Under FM breakdown stage, the patches over the shoal decreased remarkably (Figure 11d), although the FM still continued to propagate near CSWM at 20:00, 12 August. The channel in the lower reach of the North Passage was then covered by the FM, with a thickness in the range of 0.3 to 1.35 m (Figure 11d). Most of the FM was then limited to the navigation channel.

## 6. Discussions

### 6.1. Contributions of Source and Sink Terms

The formation and breakdown of the FM were mainly determined by the source and sink terms in equation 13, including Settling, Entrainment, Erosion, and Dewatering. The spatial distributions of these terms and their sum at T2, for example, are shown in Figure 16. The results showed an active sediment exchange between the two interfaces in the North Passage. The FM existed only in a narrow channel from CS4M to CS10M, whereas no FM was detected in the other regions. The sediment settling had a spatially smoothed distribution around the no-FM region (Figure 16a). The SSC was mainly controlled by conventional sediment dynamics; only settling and erosion occurred in this region. Without the FM, the Entrainment equaled the Erosion (Figures 16b and 16d). This situation applied to most of the North Passage. At T2, the water velocity was relatively strong in the channel between CSWM and CS4M (Figure 10). The bottom shear stress produced the strong sediment erosion around CSWM and near the main channel (Figure 16d). A difference between the entrainment and bed erosion only occurred around the FM-covered region, mainly in the channel around CS4M (Figure 16b). A significant entrainment process was found around the landward tip of the FM near CS4M. At this time, the FM flow at CS4M was weak, and the upper ambient flow was relatively strong (Figure 13b). According to equation 15, the entrainment was highly related with the magnitude of $u - u_m$. The large velocity difference between the suspension layer and the FM suggested strong turbulent mixing and active mass exchange at the interface, which led to a relatively strong entrainment around the landward tip. On the other hand, the FM flow was slow, which was insufficient to produce the bed erosion in the FM-covered channel (Figure 16d). Dewatering only occurred beneath the FM (Figure 16c). The sum of these four terms showed a similar distribution pattern (Figure 16e). The upper reach of the North Passage

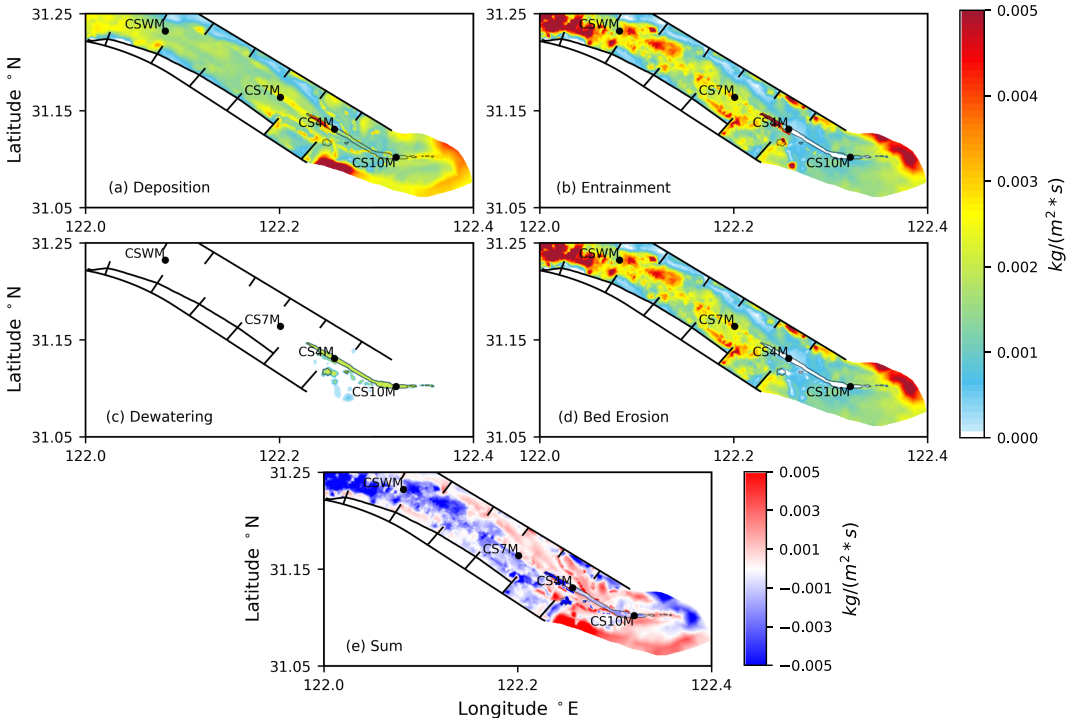


**Figure 16.** Spatial distributions of the deposition (a), entrainment (b), dewatering (c), and erosion (d) occurring at the FM-bed and FM-suspension interfaces at the time T2. The sum of these four source/sink terms is also included (e). The black solid curves outline the coverage of the FM.

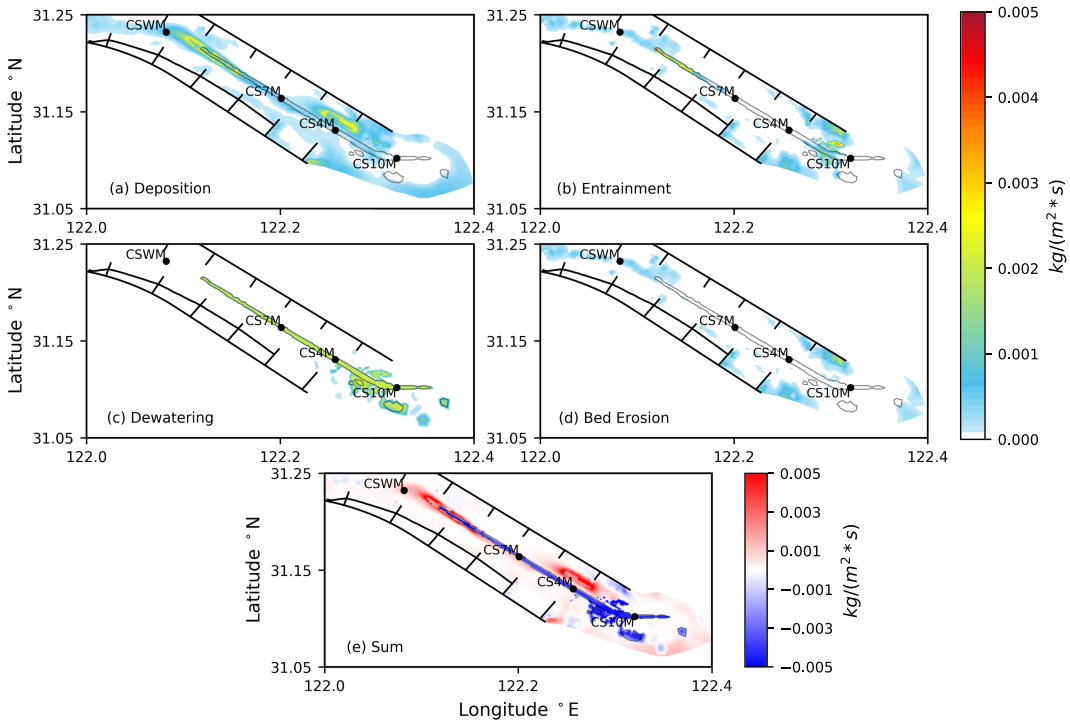


**Figure 17.** Same as Figure 16 except at the time T4.

was dominated by the sink effect, suggesting that the sediment had mainly eroded into the suspension layer, which was unfavorable to the FM formation (Figure 16e). The lower reach was mainly controlled by the source effect, suggesting that the sediment settling dominated. The shallow shoals within the groynes also had a significant positive net contribution to the FM (Figure 16e). These shallow shoals could apparently also accumulate sediment, making them a potential place for the FM formation.

During the breakdown stage, T4, the source and sink terms had quite a different distribution than that in the growth stage (Figure 17). The sediment settling became weak compared with the conditions at T2 (Figure 17a). In the velocity-decreasing phase during the neap tide, the tidal flow was weak at T4, which led to the weak erosion and entrainment. The entrainment was also weak above the FM-covered area, except during the landward trip between CSWM and CS7M (Figure 17b). It had similar dynamics to those at T2, with a larger FM flow velocity at the extension edge and a weaker ambient flow (Figure 13d). It produced a significant amplitude of $u - u_m$, leading to an entrainment. Dewatering was uniform throughout the FM coverage. According to equation 17, the dewatering process was only related with the consolidation rate and FM concentration. In this study, since these two attributes were spatially uniform and temporally constant parameters, they inevitably produced the uniformly dewatering at the FM-bed interface. The sum of the four source/sink terms demonstrated that the net effect was negative at T4 (Figure 17e). It suggested that dewatering and entrainment dominated the breakdown process of the FM. In the following spring tide, the entrainment's influence strongly grew as a result of energetic tidal currents and enhanced mixing. With the joint effect of the dewatering and tide-induced entrainment, the FM eventually experienced a strong breakdown process in the spring tide.

Additionally, the sensitivity experiments indicated that the FM model was sensitive to the dewatering process (Figure 9), which depended on the product of the dewatering velocity and FM concentration. In this study, these two parameters were configured as constant numbers in the simulation. To improve the model performance, further in situ field measurements should be made to provide the model with more realistic spatially and temporally nonuniform parameters.

### 6.2. Contribution of Bed Property on the Mud Source

Ultimately, the bed-stored sediment was the major mud source for the FM. The distribution and variation of this source were controlled by external driving forces, such as tidal mixing, shear stress, and the wave-current interaction-produced bottom drag coefficient. The sediment properties of the seabed influenced the amount of sediment that eroded into the water column, which functioned as a final material source for the FM in the subsequent rapid sediment settling. Fine grain size sediment was the major component in the FM (Winterwerp, 1999). Therefore, the occurrence of the FM was dynamically related with the seabed sediment size and classification.

The North Passage was dominated by fine sediment with a grain size smaller than 20 μm (Figure 4a), suggesting an abundant mud source for the FM formation. The lower reach of the North Passage had a clay content >20%, even >30% around the seaward outlet near CS4M and CS10M (Figure 4b). This outlet region provided the adequate clay materials for the FM formation, as well as the upper suspension. Energetic tidal conditions produced the strong sediment erosion into the water column. With moderate and weak vertical mixing during the transition from the spring tide to the neap tide, the sediment suspension accumulated in the near-bottom layer and formed the FM. Since the seabed provided the necessary material availability for the sediment source of the FM layer, the seabed sediment property was an essential factor during the formation stage of the FM.

### 6.3. Local Dredging Impact

Significant FM formation between CS9 and CS2 (Figure 3) was observed. However, the numerical model failed to reproduce this (Figure 9a). The FM thickness at that area was about 75 cm, and its formation did not follow the mechanism discussed above. The FM was only detected in a narrow region. The model did not capture any local formation or lateral transport of the FM into this region. This difference was probably related with the anthropogenic effect in the local channel. To maintain an adequate cargo-shipping depth, dredging is ongoing along the navigational channel as a daily routine activity (Dai et al., 2013; Pan et al., 2012; Z. B. Wang et al., 2015). Some particular locations within the groyne area are selected as temporary storage for the dredged mud. One groyne region between N3 and N4 happened to be a storage site. These sediments

would eventually be pumped onto the nearby Hengsha Shoal for land reclamation (Liu et al., 2011). Part of this stored mud had the chance to return to the main channel. During the typhoon passage, the surface wave was not high in the main channel. According to the simulation results, $H_s$ around CS2 was about 0.5 m. It was not sufficient to produce a high-bottom shear stress but was adequate to produce a significant wave-induced stress and disturbance on the shallow shoal between N3 and N4. Previous tripod measurements found a notable cross-channel southward flow (Ge et al., 2018), which potentially carried the mud from the shallow shoal within the groynes to the deep channel. This flow pattern and the storage of dredging within the shoal could have played an important role in the FM formation around CS2.

### 6.4. Role of Typhoon Wind in Modulating Estuarine Stratification

In this study, the typhoon-enhanced stratification played a crucial role in the formation of the FM the estuarine channel. The mechanism relied on the role of the wind in modulating estuarine stratification, particularly under the storm-induced extreme weather condition. Previous studies in the estuaries of Cape Cod, USA, found that the estuarine flow could be weakened by an onshore wind, with the increase of the along-estuary salinity gradient due to the freshwater accumulation; the outflow from the estuarine channel could be enhanced by an offshore wind, resulting in the decrease of the along-estuary salinity gradient (Geyer, 1997). In the case of this study, the typhoon path was on the south side of the North Channel (Figure 1a). With the counterclockwise swirling pattern of the typhoon wind, the estuarine channel experienced an onshore wind, which increased the estuarine stratification much in the same manner as those shown in Figures 13 and 15.

This mechanism was also observed in the York River Estuary (Scully et al., 2005) and confirmed in idealized model experiments to examine the axial wind effects on stratification (S. Chen & Sanford, 2009). The relative importance between the wind stress and baroclinic pressure gradient force could be quantitatively estimated using a nondimensional parameter named the number (S. Chen & Sanford, 2009; Geyer, 1997; Monismith, 1986):

$$W = \frac{\tau_{wx} L}{\Delta \rho g H^2} \tag{18}$$

where $\tau_{wx}$ is the along-channel wind stress (positive in onshore wind), $L$ is the length of the estuarine or channel (70 km), $\Delta\rho$ is the density change over $L$, $g$ is the parameter for the gravitational acceleration, and $H$ is the averaged depth of the channel. In our case, with a typhoon-induced maximum wind of ~20 m/s at the site of CJK (Figure 7), $W$ was 1.98, representing the strong importance of the wind stress on the baroclinic pressure gradient force and its induced vertical density stratification. Under this mechanism, the typhoon path was a critical factor that determined the onshore or offshore wind at specific locations or more generally a channel or an estuary.

## 7. Conclusion

A comprehensive field campaign in the area of maximum turbidity in the North Passage of the Changjiang River Estuary detected the FM formation after Typhoon Haikui. The observations showed that a greater FM was developed in both the horizontal and vertical extents during the neap tide. The SSC was generally above 50 g/L, with a maximum of 87.8 g/L. The FM was predominantly in the near-bottom layer within the navigational channel. The spatial and temporal variability of the FM cooccurred with a strong saltwater intrusion, which led to the pronounced stratification in the neap tide. Acoustic measurements revealed that the FM occurred mainly in the lower reach of the North Passage, with a maximum thickness of ~0.9 m.

A two-layer model, with an upper suspension layer and a lower FM layer, reproduced the formation, transport, and breakdown of the FM over a period during Typhoon Haikui. This approach was based on the unstructured grid FVCOM model with the inclusion of the fully nonlinear wave-current interaction. The model successfully revealed that the typhoon strongly intensified the salinity-induced stratification level in the outlet region, which essentially led to the FM formation. The simulation indicated that the FM formed under increased stratification about 1 day before the typhoon landed and reached its maximum 2 days after the typhoon passed. Subsequent weak mixing in the neap tide sustained the FM. In the subsequent period of moderate and spring tides, when the mixing in the upper water column became stronger, the FM entered its

breakdown stage. The simulation results also showed that the FM experienced a strong propagation process. It formed mainly in the outlet region and gradually extended landward along the channel under the influence of the saltwater intrusion. Eventually, it occupied nearby shallow shoal areas outside the North Passage. The boundary of the FM landward extension had an active entrainment as a result of a larger velocity difference between the FM and ambient tidal flow.

**Acknowledgments**
J. Ge, P. Ding, K. Ke, and J. Yi are supported by the National Natural Science Foundation of China (Grant 41776104) and National Key R&D Program of China (Grants 2016YFA0600903, 2017YFE0107400). Z. Wang is supported by the KNAW Project (Grant PSA-SA-E-02). C. Chen is supported by his Montgomery Charter Chair fund for his time and also the travel fund from the International Center for Marine Studies (ICMS) at Shanghai Ocean University (SHOU). The two-layer model used in this study has been included in the latest FVCOM version 5.0, which will be freely available (https://code.fvcom.org/medm). All data sets used in this work are publicly available online (https://figshare.com/s/6c5b19b2f9dab52f87fe). The authors would like to thank two anonymous reviewers and Editor Chris Sherwood for providing constructive comments and suggestions on the manuscript.

## References

Chen, C., Beardsley, R., Cowles, G., Qi, J., Lai, Z., Gao, G., et al. (2013). *An unstructured grid, finite-volume community ocean model FVCOM user manual, SMAST/UMASSD-13-0701*. Mass. [Available at: New Bedford. https://fvcom.smast.umassd.edu/fvcom/

Chen, C., Beardsley, R. C., & Cowles, G. (2006). An unstructured grid, finite-volume coastal ocean model (FVCOM) system, special issue entitled "advance in computational oceanography". *Oceanography*, *19*(1), 78–89. https://doi.org/10.5670/oceanog.2006.92

Chen, C., Liu, H., & Beardsley, R. C. (2003). An unstructured, finite-volume, three-dimensional, primitive equation ocean model: Application to coastal ocean and estuaries. *Journal of Atmospheric and Oceanic Technology*, *20*(1), 159–186. https://doi.org/10.1175/1520-0426(2003)020<0159:AUGFVT>2.0.CO;2

Chen, C., Xue, P., Ding, P., Beardsley, R. C., Xu, Q., Mao, X., et al. (2008). Physical mechanism for the offshore detachment of the Changjiang diluted water in the East China Sea. *Journal of Geophysical Research*, *113*, C02002. https://doi.org/10.1029/2006JC003994

Chen, J., Li, D., Chen, B., Hu, F., Zhu, H., & Liu, C. (1999). The processes of dynamic sedimentation in the Changjiang Estuary. *Journal of Sea Research*, *41*(1–2), 129–140. https://doi.org/10.1016/S1385-1101(98)00047-1

Chen, J.-L., Ralston, D. K., Geyer, W. R., Sommerfield, C. K., & Chant, R. J. (2018). Wave generation, dissipation, and disequilibrium in an embayment with complex bathymetry. *Journal of Geophysical Research-Oceans*, *123*(11), 7856–7876. https://doi.org/10.1029/2018JC014381

Chen, S. N., & Sanford, L. P. (2009). Axial wind effects on stratification and longitudinal salt transport in an idealized, partially mixed estuary. *Journal of Physical Oceanography*, *39*(8), 1905–1920. https://doi.org/10.1175/2009JPO4016.1

Corbett, D. R., Dail, M., & Mckee, B. (2007). High-frequency time-series of the dynamic sedimentation processes on the western shelf of the Mississippi River Delta. *Continental Shelf Research*, *27*(10–11), 1600–1615. https://doi.org/10.1016/j.csr.2007.01.025

Dai, Z., Liu, J. T., Fu, G., & Xie, H. (2013). A thirteen-year record of bathymetric changes in the North Passage, Changjiang (Yangtze) estuary. *Geomorphology*, *187*(C), 101–107. https://doi.org/10.1016/j.geomorph.2013.01.004

De Nijs, M. A. J., & Pietrzak, J. D. (2011). An explanation for salinity-and SPM-induced vertical countergradient buoyancy fluxes. *Ocean Dynamics*, *61*(4), 497–524. https://doi.org/10.1007/s10236-011-0375-x

Eidam, E. F., Ogston, A. S., & Nittrouer, C. A. (2019). Formation and removal of a coastal flood deposit. *Journal of Geophysical Research: Oceans*, *124*, 1045–1062. https://doi.org/10.1029/2018JC014360

Ge, J., Chen, C., Qi, J., Ding, P., & Beardsley, R. C. (2012). A dike-groyne algorithm in a terrain-following coordinate ocean model (FVCOM): Development, validation and application. *Ocean Modelling*, *47*(C), 26–40. https://doi.org/10.1016/j.ocemod.2012.01.006

Ge, J., Ding, P., Chen, C., Hu, S., Fu, G., & Wu, L. (2013). An integrated East China Sea–Changjiang Estuary model system with aim at resolving multi-scale regional–shelf–estuarine dynamics. *Ocean Dynamics*, *63*(8), 881–900. https://doi.org/10.1007/s10236-013-0631-3

Ge, J., Shen, F., Guo, W., Chen, C., & Ding, P. (2015). Estimation of critical shear stress for erosion in the Changjiang Estuary: A synergy research of observation, GOCI sensing and modeling. *Journal of Geophysical Research: Oceans*, *120*, 8439–8465. https://doi.org/10.1002/2015JC010992

Ge, J., Zhou, Z., Yang, W., Ding, P., Chen, C., Wang, Z. B., & Gu, J. (2018). Formation of concentrated benthic suspension in a time-dependent salt wedge estuary. *Journal of Geophysical Research: Oceans*, *123*, 8581–8607. https://doi.org/10.1029/2018JC013876

Geyer, W. R. (1993). The importance of suppression of turbulence by stratification on the estuarine turbidity maximum. *Estuaries*, *16*(1), 113–125. https://doi.org/10.2307/1352769

Geyer, W. R. (1997). Influence of wind on dynamics and flushing of shallow estuaries. *Estuarine, Coastal and Shelf Science*, *44*(6), 713–722. https://doi.org/10.1006/ecss.1996.0140

Geyer, W. R., & Ralston, D. (2011). The Dynamics of Strongly Stratified Estuaries. In E. Wolanski & D. McLusky (Eds.), *Treatise on Estuarine and Coastal Science* (Vol. 2, pp. 37-51). https://doi.org/10.1016/B978-0-12-374711-2.00206-0

Guan, W. B., Kot, S. C., & Wolanski, E. (2005). 3-D fluid-mud dynamics in the Jiaojiang Estuary, China. *Estuarine, Coastal and Shelf Science*, *65*(4), 747–762. https://doi.org/10.1016/j.ecss.2005.05.017

Hale, R. P., Ogston, A. S., Walsh, J. P., & Orpin, A. R. (2014). Sediment transport and event deposition on the Waipaoa River Shelf, New Zealand. *Continental Shelf Research*, *86*(C), 52–65. https://doi.org/10.1016/j.csr.2014.01.009

Hsu, T.-J., Ozdemir, C. E., & Traykovski, P. A. (2009). High-resolution numerical modeling of wave-supported gravity-driven mudflows. *Journal of Geophysical Research*, *114*(C5), F04016, C05014–F04015. https://doi.org/10.1029/2008JC005006

Knoch, D., & Malcherec, A. (2011). A numerical model for simulation of fluid mud with different rheological behaviors. *Ocean Dynamics*, *61*(2-3), 245–256. https://doi.org/10.1007/s10236-010-0327-x

Le Hir, P., Bassoullet, P., and Jestin, H. (2000). Application of the continuous modeling concept to simulate high-concentration suspended sediment in a macrotidal estuary. In Proceedings in Marine cience (Vol. 3, pp. 229–247). Elsevier. https://doi.org/10.1016/S1568-2692(00)80124-2

Li, L., He, Z., Xia, Y., & Dou, X. (2018). Dynamics of sediment transport and stratification in Changjiang River Estuary, China. *Estuarine, Coastal and Shelf Science*, *213*, 1–17. https://doi.org/10.1016/j.ecss.2018.08.002

Liu, G., Zhu, J., Wang, Y., Wu, H., & Wu, J. (2011). Tripod measured residual currents and sediment flux: Impacts on the silting of the Deepwater Navigation Channel in the Changjiang Estuary. *Estuarine, Coastal and Shelf Science*, *93*(3), 192–201. https://doi.org/10.1016/j.ecss.2010.08.008

McAnally, W. H., Friedrichs, C., Hamilton, D., Hayter, E., Shrestha, P., Rodriguez, H., et al., & ASCE Task Committee on Management of Fluid Mud (2007). Management of fluid mud in estuaries, bays, and lakes. I: Present State of Understanding on Character and Behavior. *Journal of Hydraulic Engineering*, *133*(1), 9–22. https://doi.org/10.1061/(ASCE)0733-9429(2007)133:1(9)

Monismith, S. G. (1986). An experimental study of the upwelling response of stratified reservoirs to surface shear stress. *Journal of Fluid Mechanics*, *171*(1), 407–439. https://doi.org/10.1017/S0022112086001507

Ogston, A. S., Cacchione, D. A., Sternberg, R. W., & Kineke, G. C. (2000). Observations of storm and river flood-driven sediment transport on the northern California continental shelf. *Continental Shelf Research*, *20*(16), 2141–2162. https://doi.org/10.1016/S0278-4343(00)00065-0

Pan, L., Ding, P., & Ge, J. (2012). Impacts of deep waterway project on morphological changes within the North Passage of the Changjiang Estuary, China. *Journal of Coastal Research*, *284*, 1165–1176. https://doi.org/10.2112/JCOASTRES-D-11-00129.1

Pu, X., Shi, J. Z., Hu, G.-D., & Xiong, L.-B. (2015). Circulation and mixing along the North assage in the Changjiang River estuary, China. *Journal of Marine Systems*, *148*(C), 213–235. https://doi.org/10.1016/j.jmarsys.2015.03.009

Qi, J., Chen, C., Beardsley, R.C., Perrie, W., Cowles, G. W., & Lai, Z. (2009). An unstructuredgrid finite-volume surface wave model (FVCOM-SWAVE): Implementation, validations and applications. *Ocean Modelling*, *28*(1), 153–166. https://doi.org/10.1016/j.ocemod.2009.01.007

Ren, J., & Wu, J. (2014). Sediment trapping by haloclines of a river plume in the Pearl River Estuary. *Continental Shelf Research*, *82*(c), 1–8. https://doi.org/10.1016/j.csr.2014.03.016

Restrepo, J. C., Schrottke, K., Traini, C., Bartholomae, A., Ospino, S., Ortíz, J. C., et al. (2018). Estuarine and sediment dynamics in a microtidal tropical estuary of high fluvial discharge: Magdalena River (Colombia, South America). *Marine Geology*, *398*, 86–98. https://doi.org/10.1016/j.margeo.2017.12.008

Scully, M. E., Friedrichs, C., & Brubaker, J. (2005). Control of estuarine stratification and mixing by wind-induced straining of the estuarine density field. *Estuaries*, *28*(3), 321–326. https://doi.org/10.1007/BF02693915

Traykovski, P., Geyer, W. R., Irish, J. D., & Lynch, J. F. (2000). The role of wave-induced density-driven fluid mud flows for cross-shelf transport on the Eel River continental shelf. *Continental Shelf Research*, *20*(16), 2113–2140. https://doi.org/10.1016/S0278-4343(00)00071-6

Traykovski, P., Trowbridge, J., & Kineke, G. (2015). Mechanisms of surface wave energy dissipation over a high-concentration sediment suspension. *Journal of Geophysical Research: Oceans*, *120*, 1638–1681. https://doi.org/10.1002/2014JC010245

Wan, Y., Roelvink, D., Li, W., Qi, D., & Gu, F. (2014). Observation and modeling of the storm-induced fluid mud dynamics in a muddy-estuarine navigational channel. *Geomorphology*, *217*, 23–36. https://doi.org/10.1016/j.geomorph.2014.03.050

Wan, Y., & Wang, L. (2017). Numerical investigation of the factors influencing the vertical profiles of current, salinity, and SSC within a turbidity maximum zone. *International Journal of Sediment Research*, *32*(1), 20–33. https://doi.org/10.1016/j.ijsrc.2016.07.003

Wang, L.Winter, C.Schrottke, K.Hebbeln, D. & Bartholoma, A. (2008). Modelling of estuarine fluid mud evolution in troughs of large subaqueous dune. Proceedings of the Chinese-German joint symposium on hydraulic and ocean engineering. Eigenverlag, Darmstadt, 372–379.

Wang, Z. B., van Maren, D. S., Ding, P. X., Yang, S. L., Van Prooijen, B. C., De Vet, P. L. M., et al. (2015). Human impacts on morphodynamic thresholds in estuarine systems. *Continental Shelf Research*, *111*, 174–183. https://doi.org/10.1016/j.csr.2015.08.009

Wang, Z. B. & Winterwerp, J. C. (1992). A model to simulate the transport of fluid mud. Tech. Rep. Z163, WL|Delft Hydraulics, Delft, The Netherlands.

Warner, J. C., Sherwood, C. R., Signell, R. P., Harris, C. K., & Arango, H. G. (2008). Development of a three-dimensional, regional, coupled wave, current, and sediment-transport model. *Computers and Geosciences*, *34*(10), 1284–1306. https://doi.org/10.1016/j.cageo.2008.02.012

Winterwerp, J. (1999). On the dynamics of high-concentrated mud suspensions. Ph.D. thesis, Delft University of Technology

Winterwerp, J. (2002). Scaling parameters for high-concentrated mud suspensions in tidal flow. Proceedings in Marine Science, 5, 171–186.

Winterwerp, J. (2006). Stratification effects by fine suspended sediment at low, medium, and very high concentrations. *Journal of Geophysical Research*, *111*, C05012. https://doi.org/10.1029/2005jc003019

Winterwerp, J. & Van Kesteren, W. (2004). Introduction to the physics of cohesive sediment in the marine environment, developments in sedimentology 56. Series editor: T. Van Loon

Winterwerp, J. C. (2011). Fine sediment transport by tidal asymmetry in the high-concentrated Ems River: Indications for a regime shift in response to channel deepening. *Ocean Dynamics*, *61*(2-3), 203–215. https://doi.org/10.1007/s10236-010-0332-0

Winterwerp, J. C., Wang, Z. B., Kester, J. A. T. M. V., & Verweij, J. F. (2002). Far-field impact of water injection dredging in the Crouch River. *Maritime Engineering*, *154*(4), 285–296. https://doi.org/10.1680/maen.154.4.285.38905

Wu, L., Chen, C., Guo, P., Shi, M., Qi, J., & Ge, J. (2011). A FVCOM-based unstructured grid wave, current, sediment transport model, I Model description and validation. *Journal of Ocean University of China*, *10*(1), 1–8. https://doi.org/10.1007/s11802-011-1788-3

Xie, M., Zhang, W., & Guo, W. (2010). A validation concept for cohesive sediment transport model and application on Lianyungang Harbor, China. *Coastal Engineering*, *57*(6), 585–596. https://doi.org/10.1016/j.coastaleng.2010.01.003

Xue, P., Chen, C., Ding, P., Beardsley, R. C., Lin, H., Ge, J., & Kong, Y. (2009). Saltwater intrusion into the Changjiang River: A model-guided mechanism study. *Journal of Geophysical Research*, *114*, C02006. https://doi.org/10.1029/2008JC004831

Yang, S. L., Milliman, J. D., Li, P., & Xu, K. (2011). 50,000 dams later: Erosion of the Yangtze River and its delta. *Global and Planetary Change*, *75*(1-2), 14–20. https://doi.org/10.1016/j.gloplacha.2010.09.006

Yang, X., Zhang, Q., & Hao, L. (2015). Numerical investigation of fluid mud motion using a three-dimensional hydrodynamic and two-dimensional fluid mud coupling model. *Ocean Dynamics*, *65*(3), 449–461. https://doi.org/10.1007/s10236-015-0815-0